

Barium in seawater

Dissolved distribution, relationship to silicon, and barite saturation state determined using machine learning

Öykü Z. Mete^{1,2,3,4,*}, Adam V. Subhas², Heather H. Kim², Ann G. Dunlea², Laura M. Whitmore⁵, Alan M. Shiller⁶, Melissa Gilbert⁶, William D. Leavitt^{3,7}, and Tristan J. Horner^{1,2,*}

¹NIRVANA Laboratories; ²Department of Marine Chemistry & Geochemistry; Woods Hole Oceanographic Institution, Woods Hole, MA 02543, USA; ³Department of Earth Sciences, Dartmouth College, Hanover, NH 03755, USA; ⁴Now at: Department of Earth and Planetary Sciences, Harvard University, Cambridge, MA 02138, USA; ⁵International Arctic Research Center, University of Alaska Fairbanks, Fairbanks, AK 99775, USA; ⁶School of Ocean Science and Engineering, University of Southern Mississippi, Stennis Space Center, MS 39529, USA; ⁷Department of Chemistry, Dartmouth College, Hanover, NH 03755, USA

~~*Corresponding author~~ *Correspondence to: omete@fas.harvard.edu or Tristan.Horner@whoi.edu

Abstract

Barium is widely used as a proxy for dissolved ~~nutrients~~[silicon](#) and particulate organic carbon fluxes in seawater. However, these proxy applications are limited by insufficient knowledge of the dissolved distribution of Ba ([Ba]). For example, there is significant spatial variability in the ~~Ba–Si~~[barium–silicon](#) relationship, and ocean chemistry may influence sedimentary Ba preservation. To help address these issues, we developed 4,095 models for predicting [Ba] using Gaussian Process Regression Machine Learning. These models were trained to predict [Ba] from standard oceanographic observations using GEOTRACES data from the Arctic, Atlantic, Pacific, and Southern Oceans. Trained models were then validated by comparing predictions against withheld [Ba] data from the Indian Ocean. We find that a model [trained](#) using depth, ~~T, S, [O₂], [PO₄]~~[temperature, salinity, as well as dissolved dioxygen, phosphate, nitrate, and \[NO₃\]](#) as ~~predictors~~[silicate](#) can accurately predict [Ba] in the Indian Ocean with a mean absolute percentage deviation of ~~6.30~~ [6.30](#) %. We use this model to simulate [Ba] on a global basis using these same ~~six~~[seven](#) predictors in the World Ocean Atlas. The resulting [Ba] distribution constrains the ~~total~~ Ba budget of the ocean to ~~122±8×(±7)×10¹² mol~~ and ~~clarifies~~[reveals systematic variability in the global barium–silicon relationship between dissolved Ba and Si.](#) We also calculate the saturation state of seawater with respect to barite. [In addition to revealing systematic spatial and vertical variations, our results show](#) that the ocean below 1,000 m is, ~~on average,~~ at ~~or near saturation~~[equilibrium with respect to barite](#). We describe a number of possible applications for our model output, ranging from use in biogeochemical models to paleoproxy calibration. Our approach ~~could be extended to other trace elements with relatively minor adjustments and~~ demonstrates the utility of machine learning to accurately simulate the distributions of tracers in the sea [and provides a framework that could be extended to other trace elements.](#)

1. Introduction

Barium (Ba) is a Group II trace metal that is widely applied in studies of modern and ancient marine biogeochemistry, despite lacking a recognized biochemical function (e.g., Horner & Crockford, 2021). These applications of Ba are based on two empirical correlations relating to its dissolved and particulate cycles. The first correlation relates to the dissolved concentration of Ba, hereafter [Ba], which is strongly correlated with that of the algal nutrient silicon (Si; as dissolved silicic acid; Fig. 1; Chan et al., 1977). Unlike [Si], ambient [Ba] concentrations are faithfully recorded by a number of marine carbonates, such as planktonic (e.g., Hönisch et al., 2011) and benthic foraminifera (e.g., Lea & Boyle, 1990), surface- (e.g., Gonneea et al., 2017) and deep-sea corals (e.g., Anagnostou et al., 2011; LaVigne et al., 2011), and mollusks (e.g., Komagoe et al., 2018). Preservation of these signals means that the Ba content of carbonates can be related to the Ba content of seawater and, by extension, that of Si. Accordingly, the Ba–Si proxy has been applied to understand ocean nutrient dynamics on decadal (e.g., Lea et al., 1989) to millennial timescales (e.g., Stewart et al., 2021).

The nutrient-like distribution of dissolved Ba in seawater is thought to be sustained by the second empirical correlation, relating to cycling of particulate Ba. Particulate Ba in seawater occurs mostly in the form of discrete, micron-sized crystals of the mineral barite ($\text{BaSO}_4(\text{s})$, barium sulfate; e.g., Dehairs et al., 1980; Stroobants et al., 1991). Pelagic BaSO_4 is an ubiquitous component of marine particulate matter (e.g., Light & Norris, 2021) and constitutes the principal removal flux of dissolved Ba from seawater (Paytan & Kastner, 1996). Pelagic BaSO_4 is thought to precipitate within ephemeral particle-associated microenvironments that develop during the microbial oxidation of sinking organic matter (e.g., Chow & Goldberg, 1960; Bishop, 1988). The flux of particulate BaSO_4 to the seafloor is correlated with the flux of exported organic matter (e.g., Dymond et al., 1992; Eagle et al., 2003; Serno et al., 2014; Hayes et al., 2021). This correlation means that the accumulation rate of sedimentary BaSO_4 —or its main constituent, Ba—can be used to trace patterns of past organic matter export on timescales ranging from millenia to millions of years (e.g., Bains et al., 2000; Paytan & Griffith, 2007; Schmitz, 1987; Schroeder et al., 1997).

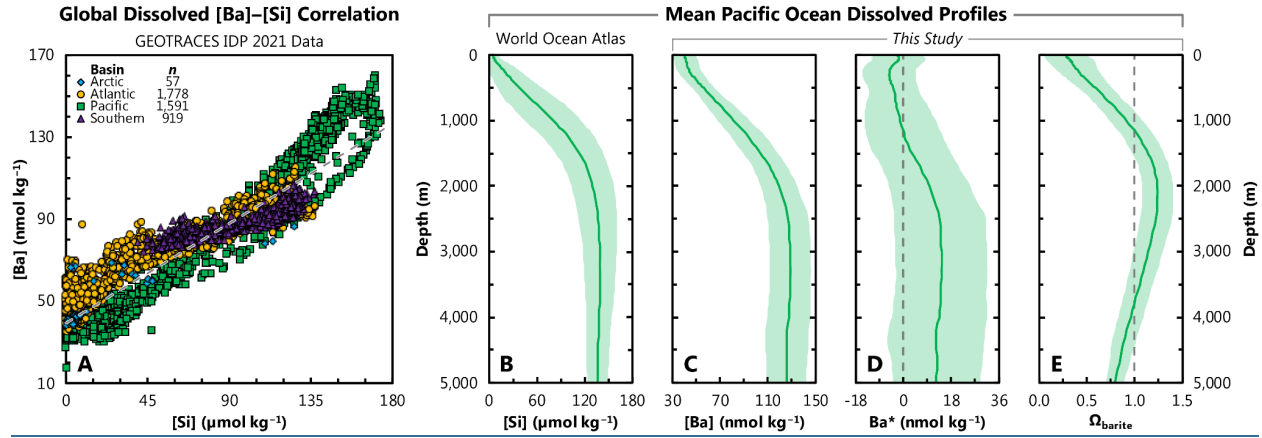


Figure 1. Distribution of barium in seawater. **A.** Property–property plot showing the 4,345 co-located, core-feature complete dissolved data used in ML model training (Sect. 2). Sample locations shown in Figure 2. Dashed line shows best-fit linear regression through these data, whereby $[Ba] = 0.54 \cdot [Si] + 39.3$. Panels **B.**, **C.**, **D.**, and **E.** show average Pacific Ocean dissolved depth profiles of $[Si]$, $[Ba]$, Ba^* , and Ω_{barite} , respectively. Solid line denotes the arithmetic mean and the shaded region encompasses one standard deviation either side of the mean. [Dashed line indicates \$Ba^* = 0\$ \(D\) and \$\Omega_{barite} = 1\$ \(E\).](#)

While the Ba-based proxies are valuable, their applications are potentially limited by insufficient knowledge of the distribution of $[Ba]$. For example, there is significant vertical and spatial variability in the Ba–Si relationship (Sect. 3.3.; [Fig. 1](#)), which we quantify using Ba^* ([barium-star](#); e.g., Horner et al., 2015):

$$Ba^* = [Ba]_{in\ situ} - [Ba]_{predicted} \quad [Eq. 1]$$

where $[Ba]_{predicted}$ is based on the Ba–Si linear regression (Fig. 1):

$$[Ba]_{predicted} = 0.54 \cdot [Si]_{in\ situ} + 39.3 \quad [Eq. 2]$$

Here, $[Si]_{in\ situ}$ has units of $\mu\text{mol kg}^{-1}$ and $[Ba]_{predicted}$ nmol kg^{-1} ; therefore, Ba^* also has units of nmol kg^{-1} . The vertical profile of Ba^* is rarely conservative ([Fig. 1D](#)) and these variations could introduce uncertainty in the reconstruction of $[Si]$ using Ba.

The relationship between sedimentary $BaSO_4$ accumulation rates and productivity also contains a significant degree of scatter (e.g., Serno et al., 2014; Hayes et al., 2021). Some of this scatter may relate to variability in $BaSO_4$ preservation, which is at least partially sensitive to ambient saturation

state, Ω_{barite} (e.g., Schenau et al., 2001; [Singh et al., 2020](#); Fig. 1). The saturation state of a parcel of water with respect to BaSO_4 is defined as:

$$\Omega_{\text{barite}} = Q / K_{\text{sp}} \quad [\text{Eq. 3}]$$

where Q is the Ba and sulfate ion product and K_{sp} is the *in situ* BaSO_4 solubility product. Discerning the importance of Ω_{barite} on BaSO_4 preservation has hitherto been challenging owing to the sparsity of *in situ* [Ba] measurements. Accurately determining the global distribution of [Ba] would be valuable for geochemists and oceanographers, and would enable a more thorough investigation of the effects of preservation on BaSO_4 fluxes and refinement of the Ba–Si nutrient proxy.

A powerful way of interrogating oceanic element distributions is through modeling. Broadly, there are two modeling approaches relevant for simulating [Ba]: mechanistic (i.e., theory driven) and statistical modeling (i.e., data driven; e.g., Glover et al., 2011). ~~Mechanistic~~ In mechanistic or process-based modeling ~~is generally viewed as the gold standard approach~~, model outputs are derived from sets of underlying equations that are based on fundamental theory. As such, mechanistic model outputs can be interrogated to obtain understanding of processes and their sensitivities. However, creating a mechanistic model of the marine Ba cycle requires embedding a biogeochemical model of BaSO_4 cycling within a computationally expensive global circulation model. Although the computational cost associated with building mechanistic models has been reduced by the development of ocean circulation inverse models (e.g., DeVries, 2014; John et al., 2020), this approach still requires detailed parametrizations of the marine Ba cycle, which do not currently exist. In contrast, statistical models are based on extracting patterns from existing data and using those relationships to make predictions. Statistical models encompass a wide variety of approaches ranging from regression analysis to machine learning (ML). Of particular interest to our study are ML models, which can make predictions without any explicit parameterizations of causal relationships. Machine learning models are computationally efficient and can be highly accurate, though they offer limited interpretability. Machine learning is increasingly being used to solve problems in Earth and environmental sciences, including simulating the dissolved distribution of tracers in the sea (e.g., for cadmium, Roshan & DeVries, 2021; copper, [Roshan et al., 2020](#); iodine, Sherwen et al. 2019; nitrogen isotopes of nitrate, Rafter et al., ~~2019~~2019; and zinc, [Roshan et al., 2018](#)).

The goal of this study is to obtain an accurate simulation of [Ba], which ML makes possible even in the absence of a process-level understanding of the marine Ba cycle. We tested thousands of ML models that were trained using quality-controlled GEOTRACES data from the Arctic, Atlantic, Pacific, and Southern Oceans, supplemented by Argo, satellite chlorophyll, and bathymetry data products (Sect. 2.). Models were tested for their accuracy by simulating [Ba] in the Indian Ocean and comparing predictions against observations made between 1977–2013. ~~Importantly, Since~~ no Indian Ocean data were seen by any of the models during training (~~Sect. 2.~~). ~~From this,~~ we are able to identify models with high generalization performance (Sect. 2.). ~~the~~ We then identify an optimal set of predictor variables ~~that results in the most accurate estimates of [Ba]~~, calculate model uncertainties, and simulate [Ba], Ba*, and Ω_{barite} on a global basis (Sect. 5.). This result will be valuable for researchers interested in marine Ba cycling, and demonstrates the utility of ML to tackle problems in marine biogeochemistry.

2. Training and testing data

Machine learning algorithms are adept at making accurate predictions of a target variable by identifying relationships between variables within large data sets. However, making accurate predictions first requires that a ML algorithm is trained on existing observations of that variable alongside a number of other parameters. These other parameters, hereafter termed features, are an important part of model training; features should encode information that may help the ML algorithm predict [Ba], otherwise their inclusion may diminish model performance. Features should also be well characterized in the global ocean, which allows ML models to make predictions in regions beyond the initial training dataset. We selected 12 model features by considering the tradeoff between feature availability and presumed predictive power (Table 1). While testing more features may have resulted in a more accurate final model, we found that many observations of [Ba] did not have corresponding data for ~~several~~ multiple features. ~~Thus;~~ thus, including more features would have meant fewer training data. ~~In subsequent sections~~ Moreover, we find that only 4–7 including more than nine features ~~are needed to accurately predict [Ba]~~ can actually diminish model performance. As such, we did not evaluate the predictive power of other ~~predictors~~ features beyond the ~~initial feature set.~~ 12 initially selected.

Table 1. List of oceanographic parameters ~~chosen~~selected as model features. The features tested were selected based on their presumed predictive power and geospatial coverage.

#	Parameter Name	Abbreviation	Units	Coverage*
1	Latitude	Lat.	degrees north (°N)	–
2	Longitude	Long.	degrees east (°E)	–
3	Sample collection depth	<i>z</i>	meters (m)	–
4	Temperature	<i>T</i>	degrees Celsius (°C)	97.44%
5	Salinity	<i>S</i>	unitless, but often written in ‘units’ of PSU or PSS	97.44%
6	Dissolved oxygen	[O ₂]	μmol kg ⁻¹	97.44%
7	Dissolved nitrate	[NO ₃ ⁻]	μmol kg ⁻¹	97.44%
8	Dissolved phosphate	[PO₄³⁻][PO ₄]	μmol kg ⁻¹	97.44%
9	Dissolved silicon (as silicic acid)	[Si(OH) ₄]	μmol kg ⁻¹	97.44%
10	Maximum monthly mean mixed-layer depth	MLD	meters (m)	88.20%
11	Mean average annual surface chlorophyll	Chl_ <i>a</i>	mg m ⁻³	93.95%
12	Bathymetry	Bathy.	meters (m)	100%

*Coverage values represent the percentage of data points within the World Ocean Atlas 2018 grid that have available data for a given parameter. Latitude, longitude, and depth have 100 % coverage as these features define the grid itself.

The 12 features used to predict [Ba] and their associated data sources are summarized in Table 1 and described below. The first three features (latitude, longitude, depth) record geospatial information that defines the location of an observation in three-dimensional space. To avoid numerical discontinuities, latitude and longitude were introduced into the model as a hyperparameter consisting of the cosine and sine of their respective values (in radians). Data for features 1–3 were included in the sample metadata. Features 4–9 encode physical (temperature, salinity) and chemical (oxygen, nutrients) information that is routinely measured alongside [Ba]. These data were generally available for the same bottle as the [Ba] measurements; however, when

that was not the case, nutrient data were taken from the corresponding location during a separate cast, or, in the case of oxygen, from linearly interpolated sensor data. The final three features are independent of depth, meaning that all samples within a given vertical profile exhibit the same value for MLD (mixed-layer depth), sea-surface chlorophyll *a*, and bathymetry. Features 10–12 were drawn from several data sources. A climatology of MLD (feature 10) was compiled using the Argo database (Holte et al., 2017). We selected maximum monthly mean MLD as the feature of interest, as this appears to be the spatiotemporal scale most relevant for influencing [Ba] distributions (Bates et al., 2017). Feature 11 represents a blended SeaWiFS and MODIS climatology of chlorophyll *a* that was obtained from the Copernicus Marine Environment Monitoring Service (CMEMS, 2021). We calculated the mean annual chlorophyll *a* for each grid cell in the data product and log transformed the data to reduce parameter weighting (e.g., Rafter et al., 2019). Data for MLD and chlorophyll *a* were extracted at the location of [Ba] observations using nearest-neighbor interpolation and their values logged in the master record. Bathymetric information (feature 12) was extracted from one of two sources. Our preferred source was the sample metadata, which generally included a value for bathymetry. For samples lacking bathymetric information, we used nearest-neighbor interpolation to extract a value from the *ETOPO5* Global Relief Model (National Geophysical Data Center, 1993). Occasionally, the *ETOPO5*-extracted bathymetry was shallower than the deepest observation of [Ba] in a given vertical profile. In such cases, the bathymetry logged in the master record was set to 1.01 times the depth of the deepest observation in that profile.

The [Ba] data from the Indian Ocean were collected from ~~a multitude of~~ [several](#), primarily pre-GEOTRACES sources (Table 2). As such, these data were generally incomplete for the 12 features used to train the ML models. Rather than using a mixture of *in situ* and interpolated data, we decided to interpolate all Indian Ocean data for parameters 4–12. Data for parameters 4–9 were linearly interpolated from the nearest vertical profile in the World Ocean Atlas 2018 (WOA; Boyer et al., 2018; García et al., 2018a; 2018b; Locarnini et al., 2018; Zweng et al., 2018) and values for MLD and chlorophyll *a* were extracted from the aforementioned data products using nearest-neighbor interpolation. Bathymetric information was obtained from either the WOA or *ETOPO5*. For the vast majority of most samples, bathymetry was taken as the arithmetic mean of the maximum depth of the nearest vertical profile in the WOA and the depth at the standard level below. For example, if the maximum depth at a station was 950 m, the bathymetry was recorded

as 975 m, which is the mean of levels 46 (950 m) and 47 (1,000 m). For profiles with a maximum depth of 5,500 m—level 102, the lowest in the WOA—bathymetry was recorded as either 5,550 m or the nearest-neighbor interpolated value from *ETOPO5*, whichever was deeper.

Table 2. Data sources. Information regarding the source of [Ba] incorporated into the master record.

Purpose	Region	Expedition ID	Data source	Data Originators (if unpublished)
Model training	South Atlantic (Meridional)	GA02	GEOTRACES IDP 2017 (Schlitzer et al., 2018)	Jose M. Godoy
	North Atlantic (Zonal)	GA03	Rahman et al., 2022	
	South Atlantic (Zonal)	GA10	Horner et al., 2015; Bates et al., 2017; Hsieh & Henderson, 2017; Bridgestock et al., 2018	
	Southern Ocean (Meridional)	GIPY04	GEOTRACES IDP 2017 (Schlitzer et al., 2018)	Frank Dehairs
	Southern Ocean (Zonal)	GIPY05	Hoppema et al., 2010	
	Arctic	GIPY11	Roeske et al., 2012	
		GN01	Whitmore et al., 2022	
	Pacific (Meridional)	GP15	GEOTRACES IDP 2021 (GEOTRACES IDP Group, 2021)	Laura Whitmore, Melissa Gilbert, Emilie Le Roy, Tristan Horner, Alan Shiller
Subtropical South Pacific (Zonal)	GP16	Rahman et al., 2022		
Model validation testing	Indian Ocean	GEOSECS	Craig & Turekian (1980)	
		INDIGO 1	Jeandel et al. (1996)	
		INDIGO 2		
		INDIGO 3		
		SR3	Jacquet et al. (2004)	
		SS259	Singh et al. (2013)	

This data ingestion process resulted in a master record containing 5,502 observations of [Ba] that also contained a corresponding value for all 12 ~~of the core~~ features ~~listed in~~ (Table 1-). The record was then split into a Pareto partition: the first partition was used for ML model training (4,345 observations, 79 % of data; Fig. 1A) and the second for model testing (1,157 data; 21 %). This partitioning was determined based on the basin from which the sample was collected; data from the Arctic, Atlantic, Pacific, and Southern Oceans were used in model training, whereas the 1,157 [Ba] data from the Indian Ocean were reserved for model testing (Table 2; Fig. 2). This location-based separation of training and testing data was chosen to minimize overfitting, which can occur when the training–testing separation is randomly assigned (see e.g., Rafter et al, 2019).~~Sect. 3.2.).~~

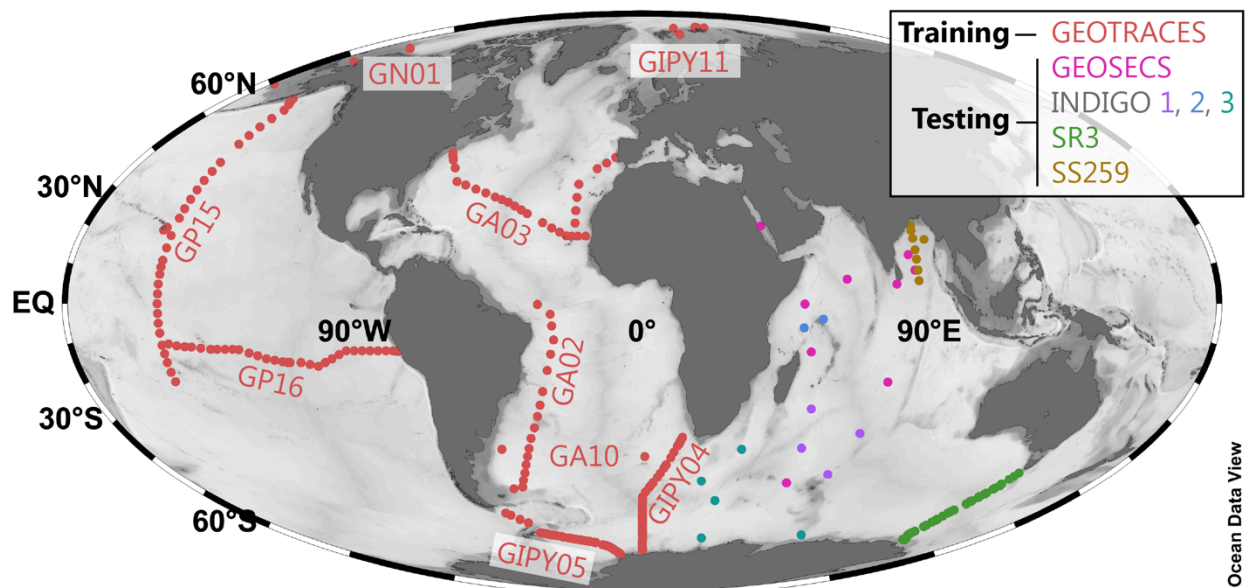


Figure 2. Geographical distribution of the training and testing data. The 4,345 core-feature complete training data (red; Fig. 1) are from the GEOTRACES 2021 Intermediate Data Product (GEOTRACES IDP Group, 2021); GEOTRACES expedition identifiers are noted next to each section. ~~Testing~~The $n = 1,157$ ~~testing~~ data from the Indian Ocean are color-coded by expedition (~~see key; $n = 1,157$~~); ~~data.~~ ~~Data~~ sources are listed in Table 2.

3. Methods

In the following subsections we discuss details of the specific ML algorithm that was used for model development (Sect. 3.1.), explain the model training and testing process (Sect. 3.2.), and describe how a global prediction of [Ba] was obtained and interrogated (Sect. 3.3.).

3.1. Algorithm selection and training

We opted for supervised ML using a Gaussian Process Regression learner, implemented in MATLAB. This particular ML algorithm is non-parametric, kernel-based, and probabilistic, which means that it does not make strong assumptions about the mapping function, can handle nonlinearities, and takes into account the effect of random occurrences when making predictions. Gaussian Process Regression algorithms are widely used in geostatistics, where it is often referred to as ‘kriging’ (e.g., Cressie, 1993; Rasmussen & Williams, 2006; Glover et al., 2011). This type of algorithm is ideal when working with continuous data that also contains a certain level of noise, such as from measurement uncertainty or oceanographic variation. ~~The basis and kernel function parameters were chosen as constant and exponential, respectively, as this combination was found to produce the most accurate predictions.~~ The MATLAB function, `fitrgp`, was used for model training. A full list of the parameter selections used in `fitrgp` is provided in Table S1. All predictors were normalized and standardized to have a mean of zero and a standard deviation of unity. This process ~~placed~~ places all parameters on the same relative range and ~~was intended to diminish~~ reduces scale dependencies.

~~A significant problem in supervised ML algorithms is overfitting: the tendency to produce highly precise fits to the training data that cannot then be generalized to new domains or environments. We attempted to minimize overfitting by performing cross-validation during model training and during model testing. First, we used holdout cross-folding during model training. Data were randomly split into two folds, one containing 80 % of the data for model training and the other 20 % withheld for model validation (i.e., the holdout fold). This holdout process was intended to eliminate models that could only generate arbitrary fits to specific subsets of the training data. In the second stage of cross-validation, we evaluated the performance of trained models by comparing predictions against a set of withheld [Ba] observations from the Indian Ocean. None of~~

~~the Indian Ocean data were seen by the models during training. This withholding was intended to help identify models that were generalizable to new environments and therefore the entire ocean (see Sect. 3.2).~~

~~3.2. Model training and testing~~

~~The training partition of the master record was used to train 4,095 different machine learning models with the goal of finding a model that could accurately simulate the global distribution of [Ba]. The number of models tested derives from the number of features investigated; each model uses a unique combination of the 12 features in Table 1 and our testing followed a factorial design whereby each feature was either enabled or disabled. This design yields a total of 2^{12} unique feature combinations (i.e., levels^{features}). Since; however, since it is not possible to train a model with no features enabled cannot be trained, the final number of unique, trainable, ML models with ≥ 1 features was $2^{12}-1=4,095$. The full experiment list is provided in Section 6. Each of the 4,095 models was trained using the same 4,345 input data and with the same function parameters described above (Sect. 3.1.). Testing every possible feature combination allowed us to select for models with the highest predictive power while minimizing overfitting. in Table S1.~~

~~3.2. In the second stage of cross validation, trained models were used to predict [Ba] for the withheld data from the Indian Ocean. Each of the 4,095 trained models were provided with the feature information that that particular model required to simulate [Ba] and the predictions recorded. The accuracy of the models was assessed by comparing ML model predictions against observed [Ba] for the Indian Ocean data ($n=1,157$) and calculating the mean absolute deviation (MAD) and mean absolute percentage deviation (MAPD). The MAD is defined as:~~

~~————MAD~~ Assessing model performance

Model performance—accuracy and generalizability—was assessed during two phases: training and testing. During model training, the 4,345 observations of [Ba] from the Arctic, Atlantic, Pacific, and Southern Oceans were randomly split into two folds: a training fold containing 80 % of the observations, and a holdout fold containing the other 20 %. Model accuracy was assessed by comparing model-predicted [Ba] against observed [Ba] for the 20 % of the data in the holdout

fold. We then performed additional testing to establish model generalizability. A significant problem in supervised ML, and particularly Gaussian Process Regression learning, is overfitting: models may fit the noise in the training data, leading to poor generalization performance (Rasmussen & Williams, 2006). Since our goal was to develop a global model of [Ba] using regional training data, we deemed it especially important to identify generalizable models. Generalizable models were identified through a testing process involving regional cross-validation; each trained model was used to predict [Ba] for the 1,157 samples from the Indian Ocean and model predictions were again compared against observations. Importantly, no [Ba] data from the Indian Ocean were seen by any of the models during training. This process helped to identify models that may have been overfit to the training data and can further be used to calculate generalization errors (Sect. 4.1).

The accuracy of trained models was determined by comparing ML model predictions against withheld data and calculating the mean absolute error (MAE) and mean absolute percentage error (MAPE), defined as:

$$\text{MAE} = \frac{\sum_{i=1}^n |[Ba]_{\text{predicted}} - [Ba]_{\text{observed}}|}{n} \quad [\text{Eq. 4}]$$

and ~~MAPD~~ as:

$$\text{MAPD} \text{MAPE} = \frac{100\%}{n} \sum_{i=1}^n \frac{|[Ba]_{\text{predicted}} - [Ba]_{\text{observed}}|}{|[Ba]_{\text{observed}}|} \sum_{i=1}^n \left| \frac{[Ba]_{\text{predicted}} - [Ba]_{\text{observed}}}{[Ba]_{\text{observed}}} \right|$$

[Eq. 5]

respectively, where n is the sample size.

Models with lower accuracy exhibit higher ~~MAD and MAPD~~ errors, whereas models with high accuracy will have lower ~~MAD and MAPD~~. For reference, the Ba-Si linear regression predicts Indian Ocean [Ba] with a ~~MAD and MAPD~~ errors. We calculated MAE and MAPE for every possible feature combination, which enables quantification of ~~6.8 nmol kg⁻¹ and 9.7 %~~, respectively (Fig. 3). These values can be considered as benchmarks for the ML models. ~~how~~ specific features affect model performance. Likewise, we calculated errors for each model on predictions made during training (i.e., for the holdout fold) and during model testing (i.e., during regional cross-validation; Fig. 3). This information is used to quantify generalization performance;

low errors for both training and testing indicate models that are both accurate and generalizable, whereas models with low training errors and high testing errors might indicate models -overfit to the training data.

3.3. Global predictions

A select number of models with low ~~MAD~~MAE and ~~MAPD~~MAPE were used to simulate [Ba] on a global basis. The process by which we selected these models is described in Section 5.1. Global simulations were performed on the same grid as the WOA, which was also used as the data source for features 1–9 (Boyer et al., 2018). The WOA is a $1^\circ \times 1^\circ$ resolution data product with around 41,000 stations that contain up to 102 depth levels spanning 0–5,500 m in 5, 25, 50, or 100 m increments. Data for features 10–12 (MLD, chlorophyll *a*, and bathymetry) were also resampled to the WOA grid using the same sources and interpolation methods as described for the Indian Ocean testing data in Section 2. Model outputs were visualized using Ocean Data View software (ODV; Figs. 4–7, 5–8; Schlitzer, 2023).

~~A selection of the most accurate models of [Ba] were then used to simulate Ba* and Ω_{barite} . The calculation~~
A selection of the most accurate models of [Ba] were then used to simulate Ba* and Ω_{barite} . Star tracers, such as Ba*, are valuable for illustrating processes that influence the cycling of elements in the ocean. First defined for N–P decoupling (N*; Gruber & Sarmiento, 1997) star tracers show variations whenever there are differences in the sources and sinks of the two elements being compared. If there are no differences in sources and sinks, the tracer will show conservative behavior because both elements share the same circulation. Barium-star is based on Ba–Si decoupling and was first defined by Horner et al. (2015). The definition of Ba* is shown in Equations 1 and 2. The coefficients in Equation 2 are based on data from the GEOTRACES 2021 Intermediate Data Product and specifically the subset of these data shown in Figure 1. These coefficients differ from previous formulations of Ba* that were based primarily on [Ba] and [Si] data from the Southern and Atlantic Oceans (e.g., Horner et al., 2015; Bates et al., 2017).
~~Calculation~~The global distribution of ML-model-derived Ba* used values of [
calculating [Ba]_{predicted} (Eq. 2) using [Si]_{in situ} from the WOA 2018 (García et al., 2018b) and]. The

values of $[\text{Ba}]_{in\ situ}$ was taken from the ML model output– and $[\text{Ba}]_{predicted}$ was subtracted from this to yield Ba^* (Eq. 1).

Values of Ω_{barite} were computed using the method described by Rushdi et al. (2000), summarized in Equation 3. ~~In~~ The numerator, Q , represents the *in situ* Ba and sulfate ion product and, in this formulation, sulfate is assumed to be conservative with respect to salinity and thus this method cannot be used to predict Ω_{barite} in restricted basins, such as the Black Sea or Caspian Sea. As ~~with~~ depends only on $[\text{Ba}]$ and $[\text{SO}_4^{2-}]$ molality. The denominator, K_{sp} , depends on T , S , and z (i.e., pressure) and is calculated in two steps: *in situ* T and S are used to calculate the stoichiometric solubility product and then this value is modified by calculating the effect of pressure on partial molal volume and compressibility, which are functions of T and z . As with the calculation of Ba^* , values of $[\text{Ba}]_{in\ situ}$ were obtained from ML models and co-located data for T , S , and ~~pressure data~~ z were extracted from the WOA (Locarnini et al., 2018; Zweng et al., 2018). Sulfate concentrations were assumed to be conservative with respect to S using $[\text{SO}_4^{2-}] = 29.26 \text{ mmol kg}^{-1}$ when salinity = 35 PSU. This latter assumption likely breaks down in certain environments (e.g., where $[\text{SO}_4^{2-}]$ reduction occurs); as such, our model is not used to predict Ω_{barite} in restricted basins, such as the Black Sea or Caspian Sea. Given that our estimates of Ω_{barite} exhibit a MAE of 0.08 (Appendix), we believe that values of Ω_{barite} between 0.92 and 1.08 are indicative of ‘perfect’ saturation with respect to BaSO_4 .

Output from the most accurate ML models was then used to calculate mean $[\text{Ba}]$ and Ω_{barite} for each basin, for a series of prescribed depth bins, and for the global ocean. This calculation was performed by weighting each cell in the model output by its volume, which ensures a fair comparison between any two points in the model output. We then subdivided the global ocean into five sub-basins: Arctic, Atlantic, Indian, Pacific, and Southern. Basin boundaries were defined as per Eakins & Sharman (2010), though we merged the Mediterranean and Baltic Seas into the Atlantic and considered the South China Sea as part of the Pacific Ocean. Neither $[\text{Ba}]$ nor Ω_{barite} were simulated in the Black or Caspian Seas and thus these regions are not included in the global mean calculations.

4. Results

4.1. **Quantifying** Factors affecting model accuracy

Here we examine ~~model accuracy and assess the role of different features in setting~~ how model performance. ~~Accuracy was assessed using the mean absolute deviation (MAD; Eq. 3), which is a measure of the correspondence between predicted and observed [Ba] for the $n = 1,157$ data from the Indian Ocean. This correspondence is illustrated for [Ba] predicted using WOA interpolated [Si] and the Ba–Si linear regression (Fig. 3A) and for ML model #3336 (Fig. 3B; Sect. 5.1.). The calculation of MAD was repeated for all 4,095 trained models and the results are summarized in Figure 3C. Of these models, 1,687 (41 %) achieve a superior MAD in the Indian Ocean compared to the Ba–Si linear regression benchmark of 6.8 nmol kg^{-1} . In general, ML models with fewer features tend to exhibit higher MAD than models with many features. However, adding more features to a model can also degrade its performance. Binned~~ influenced by the number of features, ~~the MAD of the median model decreases from 15.8 to 7.1~~ and nature of features included during training. We consider model performance in terms of accuracy and generalizability, which we quantify using MAE (Eq. 4). We first explore how the number of features influences model performance (Fig. 3). Here we see that increasing the number of features generally improves the accuracy of trained models; however, the response differs depending on whether accuracy is calculated based on comparison to the holdout fold (i.e., during model training) or to the withheld Indian Ocean data (i.e., during model testing). When considering only the holdout fold, trained models predict [Ba] with a high level of accuracy—the mean, median, and most-accurate trained models achieve a MAE of 2.4, 1.7, and 1.3 nmol kg^{-1} , respectively. Similarly, increasing the number of features almost always improves model accuracy; the MAE of the most accurate model for a given number of features decreases from 6.5 to 1.3 nmol kg^{-1} as the number of features is increased from one to five. Beyond five features, the median model MAD nine, at which point MAE plateaus; the median MAD of the 2,510 models with ≥ 6 features is 7.8 nmol kg^{-1} between 1.4–1.5 nmol kg^{-1} for models with 10–12 features (Fig. 3A).

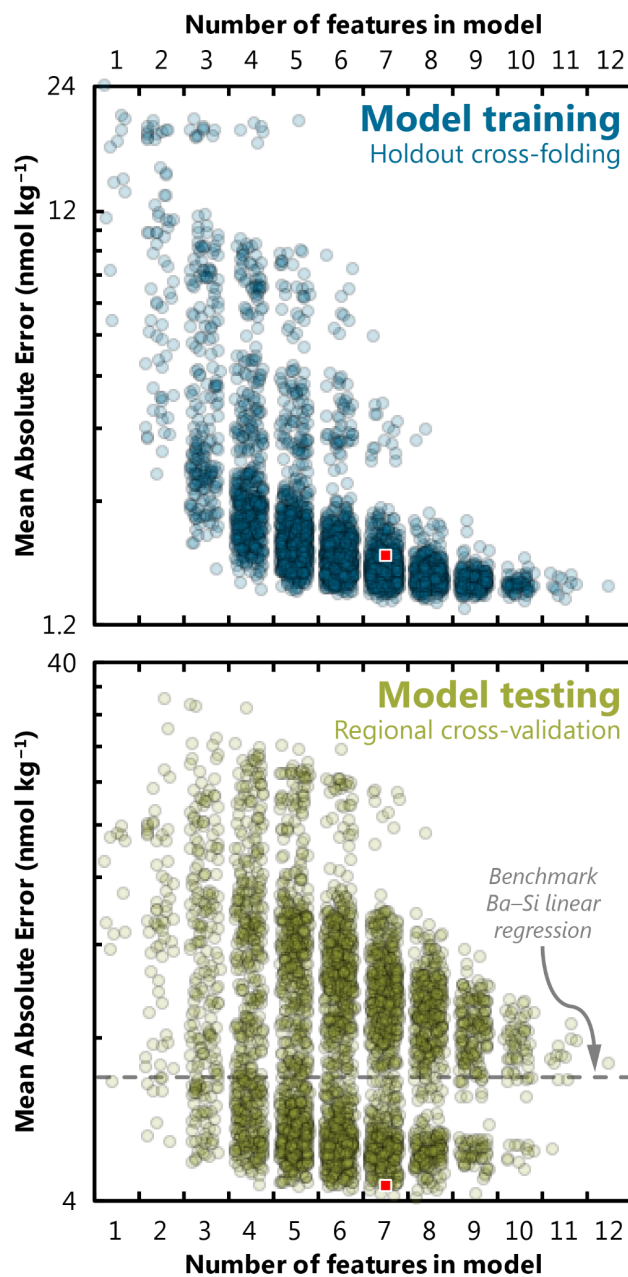


Figure 3. Effect of feature addition on ML model accuracy. Accuracy was quantified for each of the 4,095 trained models and quantified here using MAE (note log scale, which differs between panels). The accuracy of trained models is shown for random holdout cross-validation during training (top) and for regional cross-validation during testing (bottom). Square indicates the performance of our favored predictor model, #3080 (see Fig. 4, Sect. 5.1). The accuracy of the Ba–Si linear regression benchmark is shown as a dashed line in the lower panel (MAE = 6.8 nmol kg⁻¹). To illustrate data density, points have been randomly positioned within their respective bin and plotted with 80 % transparency.

Moving to the regional cross-validation, the overall performance of models is lower; the same 4,095 trained models achieve a mean, median, and most-accurate MAE for the Indian Ocean dataset of 8.8, 7.9, and 4.0 nmol kg⁻¹, respectively. For comparison, if [Ba] was estimated for these

same 1,157 Indian Ocean samples using the linear [Ba]–[Si] relationship (Fig. 1) and ambient [Si] as the only predictor, this linear model would achieve a MAE of 6.8 nmol kg⁻¹. Thus, there are 1,687 ML models that achieve a superior accuracy to existing methods for estimating [Ba], offering an improvement of as much as 41 % (Fig. 4). However, regional cross-validation also shows that the addition of more features may, in fact, degrade model performance. The MAE of the most accurate model for a given number of features decreases from 6.6 to 4.0 nmol kg⁻¹ as the number of features is increased from one to eight. As the number of features is increased from nine to twelve^{9–12}, the MAD_{MAE} of the most-accurate ML model within each bin monotonically increases monotonically from 4.1 to 7.2 nmol kg⁻¹ (Fig. 3C). Thus, the number of features necessary¹ nmol kg⁻¹. The overall lower performance of trained models during regional cross validation—and the observation that many of the feature-rich models perform worse than models with fewer features—is indicative of certain models being over-fit to the training data. Together, these observations suggest that the optimum number of features needed to accurately predict [Ba] in the Indian Ocean appears to be is between five and eight.

We then quantified the importance of different features to model performance through a feature addition analysis (Fig. 3D). For example, model #3352 contains five features: *z*, *S*, [O₂], [PO₄], and [NO₃] and achieves a MAD of 4.6 nmol kg⁻¹. Adding *T* to this model increases the number of features to six and nine.

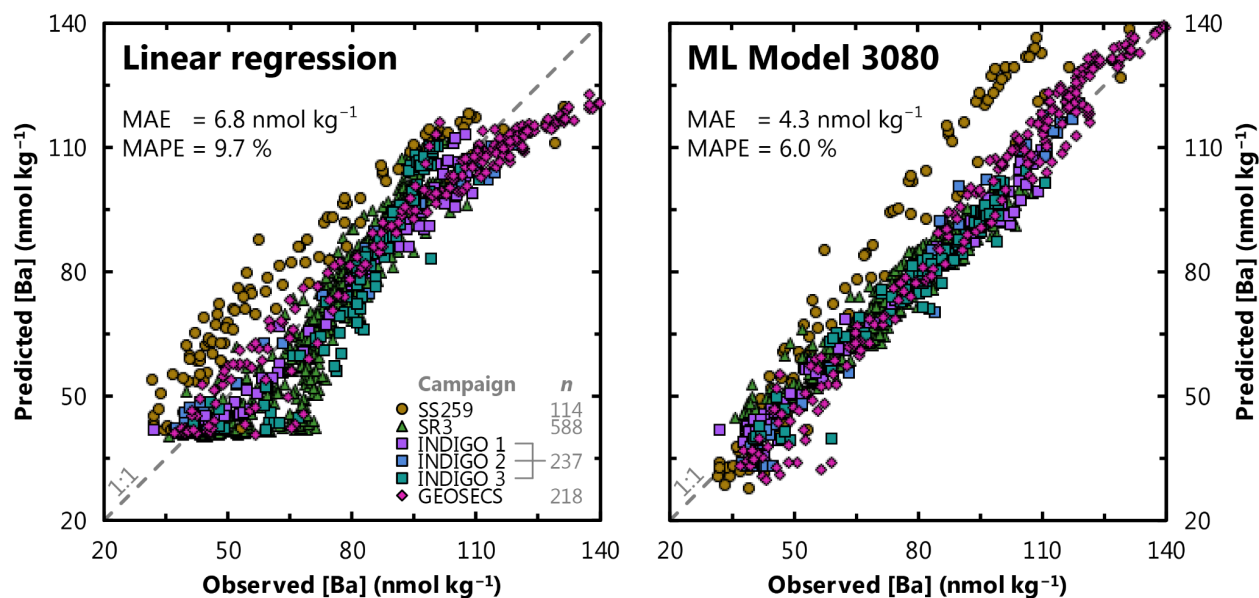


Figure 4. Comparison of existing and ML methods to estimate [Ba] in seawater. Left panel shows the performance benchmark: predicted [Ba] for the Indian Ocean testing data using the [Ba]–[Si] linear regression and ambient [Si] as the sole predictor. Right panel shows predicted [Ba] using ML model 3080, which improves on existing methods by more than 37 %. Perfect correspondence between predictions and observations is indicated by the dashed line marked '1:1'. Data locations and sources are shown in Fig. 2 and Table 2, respectively; n refers to the number of testing data for each campaign. ~~reduces~~ Mean Absolute Error (MAE; Eq. 4) and Mean Absolute Percentage Error (MAPE; Eq. 5) are noted for both models.

We also evaluated the ~~MAD to 4.4 nmol kg⁻¹~~ (Fig. 3B). ~~Since we~~ nature of the predictors used ~~at~~ to estimate [Ba]. The full factorial experiment design, ~~we were able~~ enables us to perform ~~analogous pairwise~~ comparisons between ~~the 2⁺⁺all~~ models that contained a certain feature, ~~such as T~~, and ~~the 2⁺⁺all of those~~ that did not. (Sect. 3.1). We quantified the effect of adding a feature by comparing the ~~absolute and~~ percentage change in ~~MAD~~MAE relative to the mean ~~MAD~~MAE of the two ~~models~~. ~~The likelihood that the inclusion of a given feature affected the MAD of the models~~ sets of models. This comparison was ~~then quantified using a two-tailed, paired t test~~. ~~Lower p values indicate~~ performed three times: for all 4,095 models based on the holdout cross-folded training data, for all models using the regionally cross-validated testing data, and again for the testing data, but only considering those 1,687 models that achieved a ~~higher likelihood that~~ superior accuracy compared to the [Ba]–[Si] linear regression model (Table 3).

Table 3. Feature addition analysis. Effect of ~~a~~each feature ~~significantly changed the MAD~~ on model performance for Training and Testing datasets. Model performance is quantified using MAE, thus all columns have units of nmol kg⁻¹ unless otherwise shown. The Testing analysis is further subdivided into a comparison of all models and 'good' models, meaning those that achieved superior accuracy than the Ba–Si linear regression (Fig. 1).

Feature	Training			Testing						
	All models (n = 4,095)			All models (n = 4,095)			Good models (n = 1,687)			
	Mean MAE of models with feature	Mean MAE of models without feature	Relative change in MAE	Mean MAE of models with feature	Mean MAE of models without feature	Relative change in MAE	Mean MAE of models with feature	Mean MAE of models without feature	Relative change in MAE	Share of models with feature
[Si]	1.71	3.03	-56%	7.08	10.6	-39%	5.06	5.50	-8.3%	63%
z	1.83	2.90	-45%	7.94	9.70	-20%	5.05	5.44	-7.4%	55%
[O ₂]	2.03	2.71	-29%	8.25	9.39	-13%	5.14	5.33	-3.8%	54%
T	1.78	2.96	-50%	7.61	10.0	-27%	5.17	5.31	-2.8%	59%
[NO ₃]	2.09	2.65	-24%	8.27	9.36	-12%	5.16	5.30	-2.7%	53%
[PO ₄]	2.11	2.63	-22%	8.24	9.40	-13%	5.17	5.30	-2.4%	53%
S	2.02	2.72	-29%	8.67	8.97	-3.5%	5.23	5.23	0.0%	53%
Bathy.	2.30	2.44	-6.1%	8.55	9.08	-6.0%	5.23	5.22	0.2%	51%
Chl.	2.25	2.48	-10%	8.67	8.97	-3.5%	5.24	5.22	0.4%	50%
MLD	2.31	2.43	-4.8%	8.69	8.95	-3.0%	5.24	5.21	0.5%	50%
Lat.	2.16	2.58	-18%	8.13	9.51	-16%	5.32	5.11	4.0%	54%
Long.	2.17	2.57	-17%	11.4	6.24	58%	6.45	5.19	22%	3%

This analysis ~~reveals that~~ yields three main results. When considering only the holdout cross-folded training data, the addition of any ~~one of 11 features will, on average, improve an ML model.~~ Silicate (-40%), T (-27%), and z (-20%) of the 12 features improves model performance by between -4.8 and -56 %. Excepting longitude, similar across-the-board improvements were observed when considering only the testing data, though the improvements for most features were more modest (between -3.0 and -39 %). If considering only the ‘good’ models, six features improved ~~the models the most and S, chlorophyll~~ model performance by -2.4 and -8.3 % ([PO₄], [NO₃], T, [O₂], z, and [Si]), five degraded model performance by +0.2 to +22 % (bathy., Chl. a, and MLD ~~the least (all -3 %)~~). Latitude, [PO₄], [O₂], [NO₃], and bathymetry improved the models by -16 % to -6 %. Longitude was the only feature found to degrade model performance, with a mean change in MAD of +59 %. The largest *p* value associated with these comparisons was ~~5E-25, indicating that these relationships were highly~~, lat., and long., and salinity had no significant ~~(Fig. 3D)~~ effect (Table 3).

Overall, our results indicate that between six and nine features will result in an accurate and generalizable ML model of [Ba], and that [PO₄], [NO₃], T, [O₂], z, [Si], and possibly S, are likely to be included as predictors in such a model.

4.2. Model outputs

Almost 1,700 models achieved superior accuracy compared to the Ba–Si linear regression benchmark of 6.8 nmol kg⁻¹. We winnow this list to a single model, #~~3336~~3080, in the next section. We henceforth refer to model #~~3336~~3080 as our favored predictor model, which achieves a ~~MAD~~MAE of 4.43 nmol kg⁻¹ using z, T, S, [O₂], [PO₄], [NO₃], and [NO₃Si] as predictors (Fig. ~~3B4~~). Model #~~3336~~3080 is used to simulate [Ba], Ba*, and Ω_{barite} on a global basis and to calculate whole-ocean averages. Surface plots showing the model outputs for the sea surface, 1,000 m, 2,000 m, and 4,000 m are shown in Figures ~~4~~, 5, 6, 7, and 8, respectively.

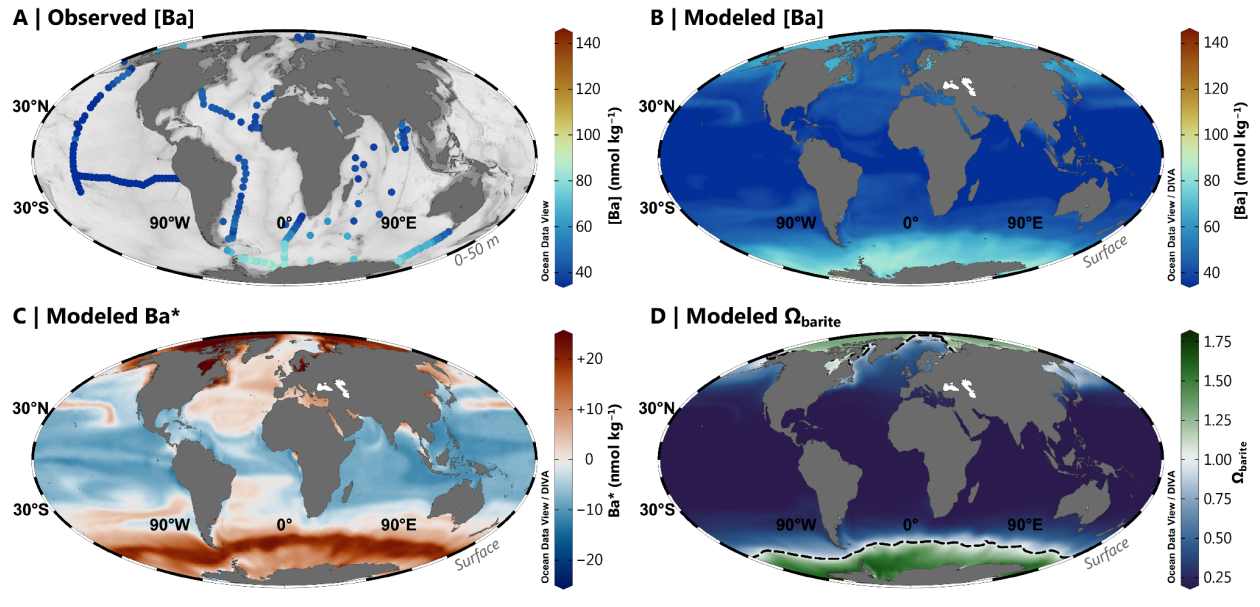


Figure 45. Barium at the sea surface. Observed [Ba] between 0–50 m (A); Model [33363080](#) [Ba] (B), Ba* (C), and Ω_{barite} (D). The dashed line in Panel D indicates the BaSO₄ saturation horizon (i.e., $\Omega_{\text{barite}} = 1.0$). Panels A and B use the *roma* color map, whereas Panels C and D use *vik* and *cork*, respectively (Crameri, 2018). Color palettes and parameter ranges are the same for the respective panels in Figure [5-76-8](#).

Figure 5. Barium at

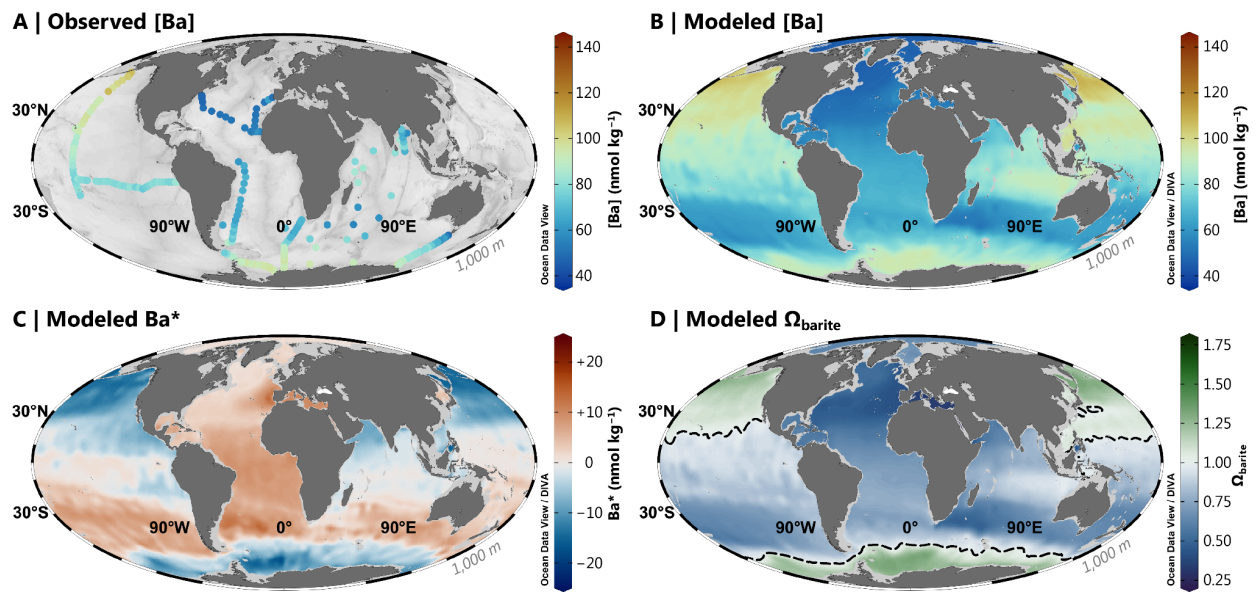


Figure 6. Barium at 1,000 m. Observed [Ba] (A); Model [33363080](#) [Ba] (B), Ba* (C), and Ω_{barite} (D). The dashed line in Panel D indicates the BaSO₄ saturation horizon.

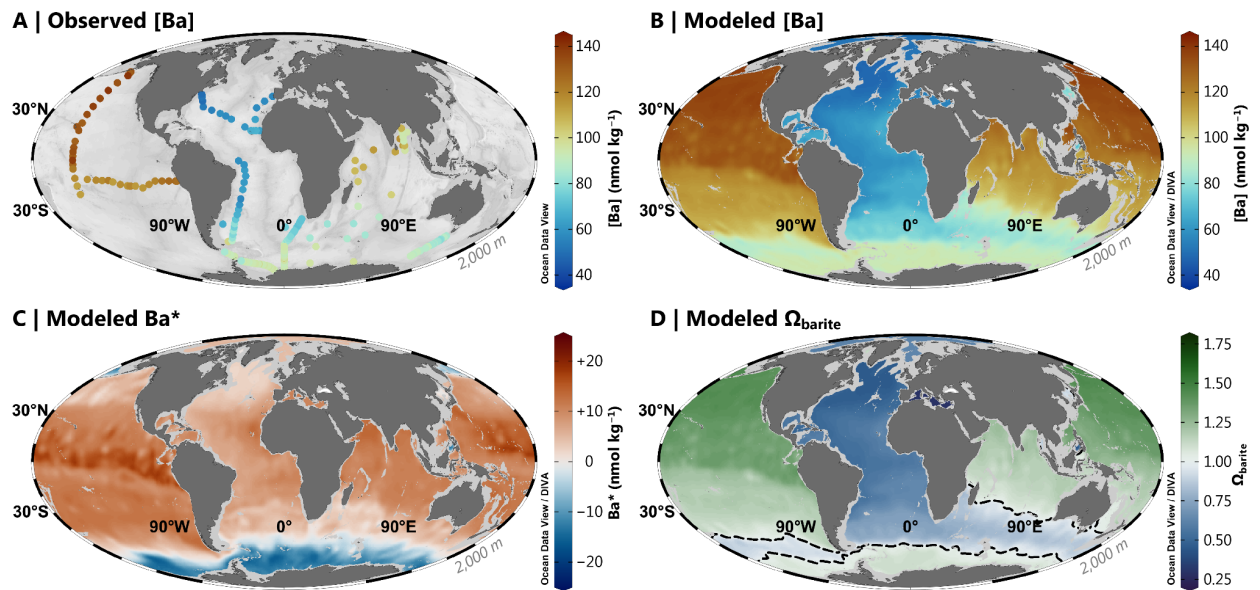


Figure 7. Barium at 2,000 m. Observed [Ba] (A); Model 3080 [Ba] (B), Ba^* (C), and Ω_{barite} (D). The dashed line in Panel D indicates the $BaSO_4$ saturation horizon.

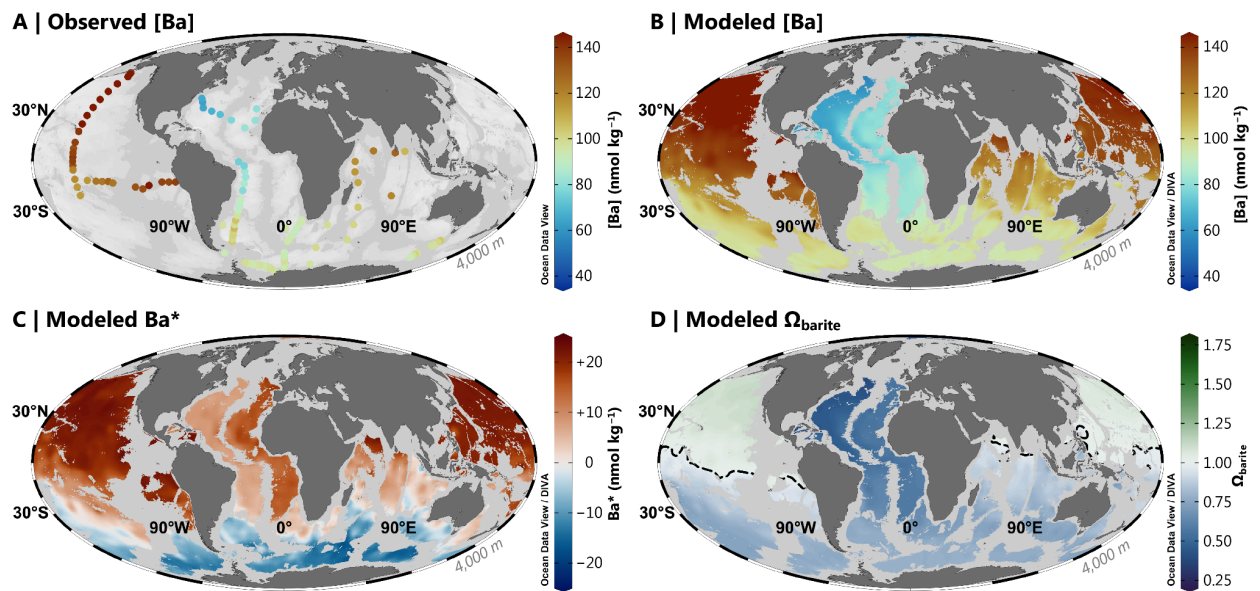


Figure 7. Barium at 4,000 m. Observed [Ba] (A); Model 33363080 [Ba] (B), Ba^* (C), and Ω_{barite} (D). The dashed line in Panel D indicates the $BaSO_4$ saturation horizon.

Model #~~3336~~3080 contains 3,305,505~~302,570~~ predictions for each of [Ba], Ba*, and Ω_{barite} . ~~Values~~ (Sect. 6). Assuming that the MAPE and MAE are good estimates of the prediction error, we estimate that modeled [Ba] ~~range from 23.3–158~~ and Ba* have uncertainties of 6.0 % and 4.3 nmol kg⁻¹, ~~with an unweighted mean of 71~~ respectively. Uncertainties on Ω_{barite} were estimated by comparison to literature data, which yields a MAE of 0.08. These estimates are discussed in more detail in Section 5.2 and the Appendix.

Modeled [Ba] ranges from 26.2–156.8 nmol kg⁻¹, and the data exhibit an unweighted mean of 72.0 nmol kg⁻¹. The range of model #3080 predictions is within the range of [Ba] encountered in the 4,345 training data (17.1–159.8 nmol kg⁻¹). This is an important consideration when assessing the accuracy of Gaussian Process Regression models, and we provide additional discussion of this point in the Supplement. Based on our formulation of Ba* (Eqs. 1, 2), Ba* varies from ~~-102.7~~27.2 to ~~+51.3~~27.9 nmol kg⁻¹ and possesses an unweighted mean of +2.24 nmol kg⁻¹. Values of Ω_{barite} vary from 0.11 to 1.7670 and exhibit an unweighted mean of 0.75. To account for the different volumes represented by each grid-cell in the ~~model~~WOA grid, we constructed a volume-weighted mean of [Ba] and Ω_{barite} for the ocean as a whole, for each ocean basin, and for a series of prescribed depth bins (Fig. 8). ~~Look~~9). Looking at the ocean as a whole, the probability density function of [Ba] roughly resembles a uniform distribution, with a mean ocean [Ba] of 89 nmol kg⁻¹ (Fig. 8A9A). Within this mean is considerable spatial and vertical variation. For example, the Arctic Ocean exhibits the lowest volume-weighted mean [Ba] of 5554 nmol kg⁻¹, whereas mean Pacific [Ba] = 106 nmol kg⁻¹. Likewise, The Indian Ocean exhibits a similar mean [Ba] ~~exceeding~~(90 nmol kg⁻¹) to the mean of the global ocean. Shallower than 1,000 m, [Ba] infrequently exceeds 100 nmol kg⁻¹ ~~rarely occurs above 1,000 m and values~~, whereas concentrations <45 nmol kg⁻¹ are ~~virtually absent~~rare below 1,000 m (Fig. 8B9B).

The probability density function of volume-weighted Ω_{barite} is ~~closer~~more similar to a normal distribution, ~~possessing~~albeit with a slight negative skew. Volume-weighted mean ~~value of~~oceanic Ω_{barite} is 0.82. The Arctic, Atlantic, and Indian Oceans are, on average, undersaturated with respect to BaSO₄, all exhibiting ~~mean~~ $\Omega_{\text{barite}} \leq 0.8182$. In contrast, the Pacific ~~Ocean is close to and~~

Southern Oceans are within uncertainty of saturation (, with mean Ω_{barite} =of 0.97), and the Southern Ocean slightly exceeds it (Ω_{barite} = and 1.04; , respectively (Fig. 8C)9C). Values of Ω_{barite} <0.25 are only found above 1,0002 are mostly restricted to the upper 250 m, whilst values of Ω_{barite} exceeding 1.455 are exceptionally rare and are, found only in the upper 1,000 m of the Southern Ocean. Lastly, Ω_{barite} tends to increase between the 0–250 m, 250–1,000 m, and 1,000–2,000 m depth bins, increasing from 0.42, to 0.6365, and 0.96, respectively. Average Ω_{barite} in the deepest bin (2,000–5,500 m) is slightly lower, with a mean value of 0.92 (Fig. 8D)9D). Given the accuracy of our model-derived Ω_{barite} predictions (0.08 to 0.10), the ocean between 1,000–5,500 m is within uncertainty of BaSO_4 equilibrium.

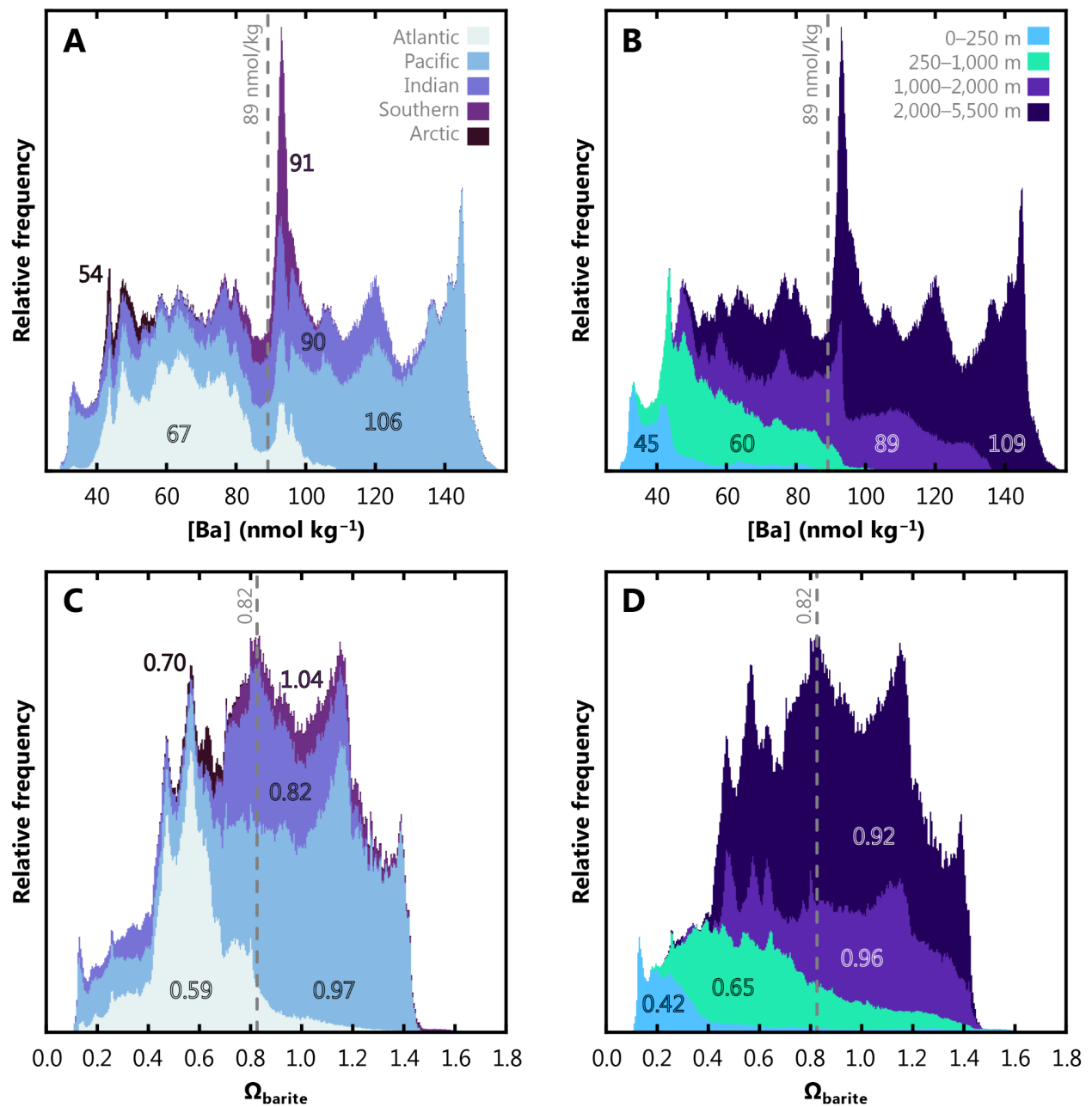


Figure 89. Stacked, volume-weighted histograms showing the relative frequency distribution of dissolved [Ba] (A, B) and Ω_{barite} (C, D) in the global ocean. The left column shows data grouped by basin, whereas and the right column is shows data grouped by a prescribed depth bin (key in B). Numbers in each panel display the mean property value for that bin. Dashed line shows the global mean.

5. Discussion

5.1. Identification of the optimal predictor model

Our results show that 1,687 of the 4,095 ML models (41%) produce more accurate predictions than the benchmark. In this case, the benchmark is predicting Indian Ocean [Ba] based on the Ba–Si linear regression and using WOA [Si] as the only predictor (Figs. 1, 3C). However, choosing *the* optimal feature combination is challenging given the sheer number of skillful ML models. Here, we winnow the list from 1,687 to a single model (#3336) by eliminating models based on the number and information content of various features. First, longitude was found to be the only feature that consistently degraded the performance of trained models (Fig. 3D). We therefore disabled this feature, eliminating 53 models. Having removed longitude, we also decided to eliminate models utilizing latitude; this decision was guided by the principle that a generalizable model should be able to predict [Ba] using only physical and/or chemical predictors, independent of where a sample is located in x – y space. This removed a further 853 models, winnowing the list to 781. After longitude, the features offering the least improvement to ML model performance were MLD and Chl. a , which improved trained models by around 3% (Fig. 3D). Indeed, the median model was degraded by 2% if Chl. a was included. Eliminating models containing either of MLD (397) or chlorophyll a (194 models) reduced the number of models exceeding the Ba–Si benchmark of 6.8 nmol kg^{-1} to 190, of which 122 utilized [Si] as a predictor. While [Si] was amongst the strongest overall predictors of [Ba] (Fig. 3D), incorporating [Si] into a trained model introduces potential circularity into the calculation of Ba^* (see Eqs. 1, 2). Moreover, the four most accurate surviving models containing [Si], models 3144, 3268, 3716, and 3732, achieve a similar MAD of 4.2 nmol kg^{-1} to our ultimately favored model #3336 (4.4 nmol kg^{-1}).

Eliminating models containing [Si] reduced the list of models to 68. Of these, 39 were eliminated as they contained ≤ 4 features, noting that our earlier analysis showed that the optimal number of features needed to accurately predict [Ba] in the Indian Ocean was between five and eight (Sect. 4.1.). Models with fewer than four features likely do not contain sufficient information to make accurate predictions in the full range of environments encountered in the Indian Ocean. Likewise, beyond eight features, trained models tended to produce worse fits to observations. We suspect that the reason is overfitting; feature-rich models can be overfit to the training data and are unable to generalize when presented with completely new environments. [Choosing a single, optimal model](#)

configuration is challenging given the sheer number of skillful ML models. Below we winnow the list from 4,095 to a single model (#3080). We base our winnowing primarily on the results of the regional cross-validation performed in the Indian Ocean, rather than from the errors determined from random holdout cross folding of the training data. We believe that there are three strong reasons for winnowing in this way. First, Gaussian Process Regression Learners tend to fit the noise in the training data, meaning that the training error is significantly lower than the generalization error (Rasmussen & Williams, 2006). Indeed, trained models showed overall lower performance during testing compared to training, which we believe is evidence of overfitting (Fig. 3, Table 3). Second, a generalizable global model should be able to make predictions in regions where it has not already learned anything about the target variable. Our regional cross-validation approach satisfies this consideration since no Indian Ocean data were seen during model training. Third, the Indian Ocean is an ideal basin for testing as it exhibits the full diversity of features expected to influence [Ba] (riverine inputs, oxygen-minimum zones, coastal upwelling, etc.) and constitutes ≈ 20 % of the global ocean volume. Likewise, the Indian Ocean captures most of the range in [Ba] seen elsewhere in the ocean (Fig. 9); this likely reflects the input of Atlantic waters through the Aughulas leakage, transport of old Pacific waters via the Indonesian Throughflow, and northward spreading of mode and intermediate waters from the Southern Ocean. We thus assume that the Indian Ocean testing errors are a good approximation of the generalization error, which we now use to winnow the list of models.

Our results show that 1,687 of the 4,095 ML models (41 %) produce more accurate predictions of [Ba] than the benchmark Ba–Si linear regression using [Si] as the sole predictor (Fig. 3, Table 3). We focus our winnowing on these 1,687 models as they are superior to existing methods for estimating [Ba] in seawater. Focusing only on these ‘good’ models reveals significant differences in the information content of the 12 features tested. For example, the inclusion of spatial information in the form of latitude and longitude significantly degrades mean model performance by between +4.0 and +22 %, respectively. While bathymetry, chlorophyll *a*, and mixed-layer depth exhibited only minor influences, they were nonetheless deleterious to mean model performance by between +0.2 to +0.5 % (Table 3). Only [PO₄], [NO₃], *T*, [O₂], *z*, and [Si] consistently improved the mean ML model, which corresponds to model #3112 (testing MAE of 4.3 nmol kg⁻¹). However, visual inspection of model #3112 output reveals that it does not reproduce expected near-shore surface plumes of elevated [Ba] close to certain major rivers (see Supplement). Though

volumetrically minor, riverine inputs are a geochemically important component of the marine Ba cycle, and the existence of nearshore Ba plumes underpins a major proxy application of Ba. Near-shore riverine influence is easily discerned by low S ; we thus explored output from model #3080, which is identical to model #3112, but includes S as a seventh feature during training. Models #3080 and #3112 exhibit identical statistical performance for the testing data (MAE = 4.3 nmol kg⁻¹; Fig. S1) and make similar predictions for mean marine [Ba] and Ω_{barite} (89 nmol kg⁻¹ and 0.82, respectively; see Supplement). The similar performance of the two models is consistent with S exerting a near-negligible impact on overall model performance (Table 3). Despite this small effect, model #3080 is better able to reproduce riverine [Ba] plumes compared to model #3112 (see Supplement). We therefore consider model #3080 to be our best estimate of marine [Ba]. Model #3080 achieves a MAPE of 6.0 %, which represents a 39 % improvement over existing methods to estimate [Ba] (Fig. 4). We henceforth consider model #3080 as our optimal predictor model, which we use to simulate [Ba], Ba*, and Ω_{barite} in Figures 5–9.

~~Thus, this winnowing process reduced the number of candidate ML models to 29. All of these models exhibited superior accuracy compared to the Ba–Si linear correlation (MAD = 6.8 nmol kg⁻¹); were not trained using longitude, latitude, MLD, chlorophyll a , or [Si]; and possessed between five and seven features. The most accurate amongst these 29 models, #3336, utilizes six features— z , T , S , [O₂], [PO₄], and [NO₃]—and achieves a MAD and MAPD in the Indian Ocean of 4.4 nmol kg⁻¹ and 6.3 %, respectively (Fig. 3B). This level of accuracy represents at least a 35 % improvement compared to predicting [Ba] in seawater using the Ba–Si linear regression. We consider model #3336 as the optimal configuration for predicting [Ba] in this study, and use this model to simulate [Ba], Ba*, and Ω_{barite} in Figure 4–8.~~

5.2. Model validation

We now explore the validity of model #~~3336~~3080 in terms of its oceanographic consistency, the sources of uncertainty that affect its accuracy, and potential limitations of the model output. We find that model #~~3336~~3080 reproduces the major known features of the marine [Ba] distribution and makes testable predictions for regions that are yet to be sampled.

5.2.1. Visual inspection of model output

Visual inspection of model output is an important component of data analysis considering the limits of statistical tests (see e.g., Anscombe, 1973). Models may produce statistically satisfactory fits to the testing data, but the oceanic realism of the output is also important to consider. Modeled [Ba] should display patterns consistent with related oceanographic properties and exhibit smooth vertical and spatial variations (Boyle & Edmond, 1975). Predicted [Ba] from model #33363080 does indeed show smooth and systematic spatial and vertical variations that also resembles sparse observations (Figs. 3–74–8).

~~There are, however, several sharp gradients in modeled [Ba], particularly at the sea surface (Fig. 3). These variations generally show an increase~~ Model #3080 also shows systematic increases in [Ba] close to land ~~and~~, especially near the mouths of major rivers ~~(Fig. 4)~~. This is reassuring given that elevated sea-surface [Ba] close to rivers is both widely reported and ~~is~~ one of the major proxy applications of Ba: reconstructing spatiotemporal patterns of terrestrial runoff by measuring the Ba:Ca ratio of carbonates (e.g., Sinclair & McCulloch, 2004; LaVigne et al., 2016). ~~Model #3336~~ For example, model #3080 correctly identifies elevated [Ba] near the Ganges–Brahmaputra (Singh et al., 2013) ~~and~~, Río de la Plata ~~outflows~~ (GEOTRACES IDP Group, 2021) ~~,~~, and Yangtze ~~outflows~~ (Cao et al., 2021). Model #33363080 also predicts elevated sea-surface [Ba] in the Gulf of Guinea (where several rivers discharge, including the Niger River; the Eastern Tropical Atlantic associated with the Congo River (Edmond et al., 1978; Zhang et al., 2023); and Volta Rivers) as well as in the Gulf of St. Lawrence (St. Lawrence River), though; see Supplement for additional details and figures). Except for the Congo River, these ~~latter~~ predictions of elevated near-shore [Ba] await corroboration. Interestingly, model #33363080 does not predict elevated ~~surface~~ [Ba] at all major ~~outflows~~ river mouths; neither the Mississippi nor Amazon Rivers are associated with significant increases in sea-surface [Ba] (see Supplement). The reasons for the lack of elevated [Ba] at near the outflow of these rivers two rivers is less clear. It is possible that the model is simply inaccurate in these regions, though we have no particular reason to believe that this is the case. Alternatively, it may reflect seasonal variations in Ba release that are not captured by our mean annual model (e.g., Joung & Shiller, 2014) ~~, or it may~~. It could also indicate that these particular rivers are not major net sources of Ba to the surface ocean, which might be the case if dissolved

[Ba is being retained in the catchment \(e.g., Charbonnier et al., 2020\) or estuary \(e.g., Coffey et al., 1997\).](#)

Overall, model #33363080 makes accurate, oceanographically consistent predictions of [Ba] in the Indian Ocean using input data from the WOA. Model #33363080 also makes a number of testable predictions of [Ba] in regions lacking direct observations. Given that these predictions were made using the same model and the same WOA inputs, we believe that it is reasonable to assume that model #33363080 output is an accurate representation of mean annual global [Ba].

5.2.2. Quantifying uncertainties

We now describe and, where possible, quantify two possible sources of uncertainty to our ML model output. Before doing so, we describe how uncertainty is quantified as well as the uncertainty of existing approaches. Certain ML models, such as Gaussian Process Regression, offer low interpretability, meaning it is not possible to assess uncertainty using a conventional error propagation. Thus, all model uncertainties are assessed *post hoc*, by comparing predictions against observations. Our preferred metrics are ~~MAD~~MAE and ~~MAPD—mean absolute deviation and mean absolute percentage deviation, defined in Equations~~MAPE (Eqs. 4 and 5, respectively). Existing approaches for estimating [Ba] result in a wide range of uncertainties. At the low end, the uncertainty associated with measuring [Ba] in seawater represents a fundamental limit to the accuracy of any model. A number of analysts report ~~relative [Ba]~~measurement uncertainties in the range of 1–2 % (e.g., Pyle et al., 2018; Cao et al., 2020). This level of intra-laboratory uncertainty is typical for [Ba] data obtained using isotope dilution–inductively coupled plasma mass spectrometry, and applies to GEOTRACES-era datasets and to much of the training data from the Indian Ocean. However, intra-laboratory uncertainty is typically much smaller than inter-laboratory uncertainty, which is often between 6–9 % (e.g., Hathorne et al., 2013). At the upper end, the benchmark Ba–Si linear regression achieves a ~~MAPD~~MAPE of 9.7 % in the Indian Ocean (Fig. 3A4). Thus, useful ML models of [Ba] should achieve ~~uncertainties~~MAPE between 1–10 %. Indeed, our favored predictor model, #33363080, achieves a ~~MAPD~~MAPE of 6.30 %.

Now we consider two factors that contribute to the observed 6.30 % uncertainty: realization uncertainty and uncertainties in the training data. The realization uncertainty stems from the fact

that two models trained on the same training dataset—even with the exact same subset of model features—will produce slightly different predictions. This is due to the holdout cross-folding process used during model training, which partitions the training dataset into [random](#) subsets (see Sect. 3.1.). ~~Because the partitioning is random~~ Thus, the training process results in a slightly different trained model each time the model is realized. We quantified the realization uncertainty by training ~~model #3336~~ [select models](#) 100 times and calculating the relative standard deviation of the different predictions of [Ba] for ~~all~~ [the 3,305,505.3 million](#) values in the output. This uncertainty is small; the median, mean, and maximum realization uncertainty was 0.03 %, 0.04 %, and 0.32 % variability in modeled [Ba].

Next we consider uncertainties in the training data. As noted above, many labs report uncertainties on [Ba] measurements of 1–2 %, while inter-laboratory differences may be up to a factor of five larger. However, this does not consider any uncertainties associated with the other physical and chemical features used to predict [Ba]. In general, these [supporting measurement](#) uncertainties should be small ~~since~~ all overboard sensors are regularly calibrated and biogeochemical properties [in GEOTRACES](#) are determined using established methods that are based on GO-SHIP best practices (Hood et al., 2010). Moreover, all GEOTRACES sections include crossover stations that are intended to facilitate intercalibration of all parameters, including those used here to predict [Ba] (Fig. 2; Cutter, 2013). The WOA, MLD, Chl. *a*, and bathymetry data products are similarly subjected to stringent quality review and so we consider it unlikely that these data contribute systematic biases. We believe that the most likely source of uncertainty relates to the fact that all predictor information used for model testing in the Indian Ocean was derived from time-averaged data products, whereas [Ba] was derived from *in situ* measurements. We made this decision because the *in situ* data were incomplete for all 12 core features (Table 1), and this would have necessitated interpolation for some features and not others. Since all models were tested using the same predictor information, the comparison process should avoid systematic errors, though this does not preclude temporal variability, described next.

5.2.3. Other considerations

We now consider four other factors that potentially contribute to the uncertainty of the model output: short- and long-term temporal variations, limitations of ML, and uncertainties regarding the thermodynamic properties of BaSO₄. Short-timescale variability in [Ba] may affect how models were evaluated, though this effect is difficult to quantify. In principle, the trained models should be able to resolve seasonal variations in [Ba] since they were trained on *in situ* physical and chemical data. In contrast, model predictions in the Indian Ocean were made using annual average physical and chemical conditions and then evaluated by comparing these predictions against *in situ* [Ba]. The temporal mismatch between Indian Ocean observations and predictions is unlikely to be significant in the deep ocean, where seasonal variations are minor and the Ba residence time is longest (e.g., Hayes et al., 2018). Seasonal variations are, however, likely to matter more for the surface ocean. We were able to minimize some of the impact of these uncertainties by using long-term averages of Chl. *a* and the maximum monthly mean MLD during model training and testing. Significant seasonal mismatches for other parameters are unavoidable given that [Ba] data are too sparse to develop a time-resolved model. We suspect that these variations are most likely to be significant for boundary sources rather than biogeochemical cycling of Ba; significant biogeochemical drawdown of surface [Ba] over seasonal timescales appears to be rare (e.g., Esser & Volpe, 2002), whereas there are large seasonal variations in river discharge that impact near-shore [Ba] (e.g., Samanta & Dalai, 2016). These suspicions could be tested using a model with better than 1×1° spatial resolution, which—in theory—is possible with model #33363080, so long as similarly high-resolution data are provided for the six predictors utilized by this model (z , T , S , [O₂], [PO₄], [NO₃], and [NO₃Si]). While it is challenging to precisely quantify seasonal uncertainties, we note that model #33363080 performs well at low [Ba], which is found mostly near the surface, where seasonal variations should ~~be exhibit the largest (Figs. 3B, 8B)-effects.~~ Likewise, seasonal variations will have only a minor effect on our calculations of global mean [Ba] or Ω_{barite} (Fig. 8).

Long-term variability in [Ba] may also influence model performance, since the testing data from the Indian Ocean were collected between 1977 (GEOSECS) and 2008 (SS259; Fig. 2). If secular changes in Indian Ocean [Ba] were occurring, we might expect models to make accurate predictions for some datasets at the expense of others. In contrast, we note that model #33363080

reproduces all testing datasets similarly well, with the exception of a subset of samples from SS259 in the deep Bay of Bengal (~~Fig. 3C~~). Here we observe that model #~~3336~~ tends to predict ~~~93080~~ predicts 18 % higher [Ba] than observed by Singh et al. (2013), ~~particularly around 2~~ for the 42 samples between 1,000–3,000 m (~~Fig. 6A~~ Figs. 4B; 7A, B). ~~However~~ Interestingly, model #~~3336~~3080 correctly predicts [Ba] at nearby GEOSECS stations 445 and 446, also in the Bay of Bengal, sampled some 31 years prior. ~~The~~ to SS259. We briefly consider three possibilities for the origin of ~~the~~ this regional model–data discrepancy. It may derive from the fact that model #3080 does not include the features needed to correctly predict [Ba] in this region these samples. We view this as the least likely possibility as model #3080 performs well for other samples from the northern Indian Ocean, including samples shallower than 1,000 m from Singh et al. (2013). Another possibility is uncertain; we speculate that it may reflect could reflect an 18 % decrease in [Ba] in the deep Bay of Bengal since the GEOSECS survey in the 1970's. Lastly, it could reflect differences in how *in situ* [Ba] was measured, noting that Singh et al. (2013) opted for standard addition ~~over~~ instead of isotope dilution. ~~Alternatively, it could reflect a ~9 % decrease in [Ba] in the deep Bay of Bengal since the 1970's.~~ We currently lack the data needed to confidently distinguish between these latter two possibilities.

A third factor concerns the limitations of ML itself. We note that no trained model was able to achieve a ~~MAPD~~ MAPE better than ~6 %. This 6 % value may represent one of three things. First, it may point toward an intrinsic limitation of Gaussian Process Regression. Other types of ML, such as Decision Trees or Artificial Neural Networks, may be able to achieve superior accuracy, though this was not investigated. Second, it may indicate that the 12 features investigated provide insufficient information about [Ba] to achieve higher accuracy. We view this as unlikely given that our earlier analysis showed that only ~~5–8~~ six–nine features were needed to accurately simulate [Ba] and that the 12 features ~~investigated~~ tested have proved useful in other studies simulating dissolved tracer distributions (e.g., Rafter et al., 2019; Sherwen et al., 2019; Roshan & DeVries, 2021). However, this does not rule out the existence of other features beyond the 12 that we tested that are more useful for predicting [Ba], only that we did not investigate them. Third, it is possible that the lowest ~~MAPD~~ MAPE of ~6 % reflects the current limit of inter-laboratory uncertainty in determining [Ba]. We note that inter-laboratory uncertainties of 6–9 % were reported for the measurement of Ba:Ca in carbonates ($n = 10$ labs; Hathorne et al., 2013). If the ~6 % ~~MAPD~~ MAPE

derives from inter-laboratory uncertainty, it is unlikely that further model refinements will improve the accuracy of [Ba] predictions: the fundamental limitation is the data, not the model.

A final source of uncertainty concerns the computation of Ω_{barite} , which contains two further sources of uncertainty: the thermodynamic model and the solubility coefficients used to calculate $\Omega_{\text{barite}}K_{\text{sp}}$. We calculated Ω_{barite} based on the computation described by Rushdi et al. (2000), and our approach yields similar values to their study and several others (e.g., Jeandel et al., 1996; (2000). This calculation Monnin et al., 1999; see Appendix). The model used by Rushdi et al. (2000) is based on BaSO_4 solubility data from Raju & Atkinson (1988), who note good agreement with the thermodynamic data of Blount (1977). These solubility data were obtained based on experimentation with lab-made, coarse-grained BaSO_4 , which is unlikely to be wholly representative of the microcrystalline BaSO_4 precipitates found in seawater. Thus, the absolute values of Ω_{barite} calculated here may be subject to eventual revision; however, the vertical (Fig. 1), spatial (Figs. 3–74–8), and whole-ocean (Fig. 89) trends in Ω_{barite} are robust. Should new thermodynamic data for marine-relevant micron-sized pelagic BaSO_4 become available, updated maps of Ω_{barite} could be ~~easily recalculated using existing model #3336 derived [Ba] data. recalculated using model #3080-derived [Ba] data.~~ Given the nature of these uncertainties, we opted to calculate prediction uncertainties for Ω_{barite} empirically by comparison to literature data (see Appendix). This yields a value between 0.08 and 0.10, similar to the 10 % prediction error reported by Monnin et al. (1999).

We can calculate Ω_{barite} to a high degree of precision; however, there are numerous uncertainties pertaining to ML-predicted [Ba], the BaSO_4 solubility coefficients used to calculate K_{sp} , and the thermodynamic model used in the computation of Ω_{barite} (Sect. 5.2.). Thus,

5.3. Barium in seawater: A global perspective ~~Model applications~~

Here we provide an overview of the main model features in [Ba], Ba^* and Ω_{barite} , then outline ~~four~~ three possible applications of the model output. ~~Predictions from model #3336 shows~~

5.3.1. Dissolved distribution of [Ba]

Model #3080 predictions show several interesting features in [Ba] (Figs. ~~4–7~~. ~~Model #33365–8~~). The model reproduces the expected nutrient-like distribution of [Ba] (Fig. 1C) and shows a general increase in [Ba] along the Meridional Overturning Circulation; volume-weighted mean [Ba] increases from 67 to ~~8890~~ to 106 nmol kg⁻¹ from the Atlantic to Indian to the Pacific Ocean, respectively. The model also predicts some variation in shallow [Ba] that follows major surface-water currents, such as a region of elevated [Ba] associated with the North Pacific Current, as well as low [Ba] in the western North Atlantic associated with the Gulf Stream (Fig. ~~4B5B~~; Talley et al., 2011). ~~Taking~~ However, these features and the processes driving them await corroboration.

Considering the ocean as a whole, we can ~~also~~ use our model ~~output~~ to calculate the total Ba inventory of ~~the ocean seawater~~. Using the mean oceanic [Ba] of 89 nmol kg⁻¹ and multiplying by the mass of seawater (1.37×10^{21} kg) yields a total inventory of 122 ± 87 Tmol Ba, whereby the range uncertainty is based on the MAPD/MAPE of model ~~#33363080~~ (6.30 %). This estimate of the total oceanic Ba inventory is ~~approximately 10~~ between 11–21 % lower than ~~previous existing~~ estimates of 145 Tmol Ba (Dickens et al., 2003; Carter et al., 2020). ~~Thus, given current estimates~~ Given the range of probable global marine Ba fluxes ~~of~~ between 18 (Paytan & Kastner, 1996) and 44 Gmol Ba yr⁻¹ (Rahman et al., 2022), our inventory estimate places the mean residence time of Ba in seawater ~~is likely~~ between 2, ~~700~~ 600–7,200 years.

~~Next we consider the main features in~~

5.3.2. The Ba*–Si relationship

We now quantify spatial and Ω_{barite} -vertical variations in the Ba–Si relationship, which we explore using Ba*. Star tracers, such as Ba*, highlight the processes affecting the distribution of a tracer by comparing it to another tracer that shares the same circulation (Gruber & Sarmiento, 1997). The concept has since been extended to study the processes affecting the distributions of many other bioactive elements, including Si (Si*, relative to N; Sarimento et al., 2004), cadmium (Cd*, relative to P; Baars et al., 2014), zinc (Zn*, relative to Si; Wyatt et al., 2014). First defined by Horner et al. (2015) for Ba, Ba* is analogous to other star tracers: it is a measure of Ba–Si decoupling whereby larger values indicate larger Ba–Si deviations relative to expected mean ocean behavior. Vertical or spatial differences in Ba and Si sources or sinks will drive variations in Ba*,

as will any Ba:Si fractionation occurring during their combined cycling. Conversely, if all Ba and Si cycling occurs in the same places (and with a fixed Ba:Si ratio), no Ba–Si decoupling will occur and Ba* will exhibit conservative behavior. Since Ba and Si are cycled by different processes and there are large vertical and spatial variations in the intensity of these processes (e.g., Bishop, 1989), significant variations in Ba* are possible. We now explore these variations.

In the surface ocean, patterns of Ba* generally resemble those of [Ba] (Fig. 4). ~~This is likely because in~~ In large parts of the ocean, surface [Si] approaches 0 $\mu\text{mol kg}^{-1}$; thus, variations in Ba* derive mostly from variations in [Ba]. ~~Barium star is, however, strongly positive in the top 200 m of the~~ This is most evident when examining regions with significant terrestrial input of Ba, such as from major rivers (Sect. 5.2.1) and from rivers and continental shelves in the Arctic (e.g., Guay & Falkner, 1998; Whitmore et al., 2022; Fig. 5A). The Southern Ocean, ~~even~~ also exhibits positive Ba*, though ~~[Si] is in the 10's of $\mu\text{mol kg}^{-1}$~~ we suspect the mechanism is different. Here we observe a belt of waters with positive Ba* $\approx +20 \text{ nmol kg}^{-1}$ ~~range-~~ centered on the Polar Frontal Zone—the region between the Antarctic Polar Front and the Subantarctic Front (Orsi et al., 1995; Fig. 5A). Silicic acid is intensely stripped from waters that transit northward through this region (e.g., Sarmiento et al., 2004), potentially contributing to elevated Ba* at the sea surface. Dissolved [Ba] and Ba* then decrease to the north of the Subantarctic front, partly driven by extensive particulate Ba formation in the frontal region (e.g., Bishop, 1989).

At 1,000 m, the Atlantic, South Pacific, and southern Indian Oceans exhibit positive Ba* around $+10 \text{ nmol kg}^{-1}$, whereas the North Pacific, Southern, and ~~Indian Oceans exhibit negative values between -10 to -20 nmol kg^{-1} , whereas the Atlantic and South Pacific~~ northern Indian Oceans are positive around $+10 \text{ nmol kg}^{-1}$ (Fig. 5). ~~Below, 1,000 m, the Southern and~~ negative between -10 to -20 nmol kg^{-1} (Fig. 6C). The positive anomalies are likely related to the northward spreading of southern-sourced intermediate waters that originate within the Polar Frontal Zone and carry positive Ba* into the low latitudes (e.g., Bates et al., 2017). In the Atlantic ~~Oceans do not exhibit significant gradients in Ba* and are~~, these values are carried all the way to the north of the basin and return as North Atlantic Deep Water with only minor modifications to Ba* ($\approx +10 \text{ nmol kg}^{-1}$; Figs. 6C, 7C, 8C). Negative Ba* in the North Pacific, Southern, and northern Indian Ocean at 1,000 m likely reflects a mixture of hydrographic processes and *in situ* processes. For example, the extensive region of negative ~~and positive down~~ Ba* in the North Pacific is closely associated

with North Pacific Intermediate Water, which originates in the Sea of Okhotsk (Talley, 1991). While the specific mechanism sustaining this particular Ba* feature is unknown, it most possibly reflects a combination of preferential removal of Ba relative to Si in the source water formation region (such as from particulate Ba formation) and weak vertical mixing in the subsurface North Pacific relative to lateral transports (e.g., Kawabe & Fujio, 2010). We suspect that the negative Ba* values seen above 1,000 m in the northern Indian Ocean originate through processes occurring internally within this basin, as the majority of the Indian Ocean below 1,000 m exhibits positive Ba*. A possible mechanism for these shallow negative Ba* anomalies may relate to the relatively weak overturning transports (Talley, 2008) and strong particulate Ba cycle north of 30 °S (Singh et al., 2013), though this awaits more detailed investigation.

Lastly, the Southern Ocean exhibits negative Ba* between -10 and -20 nmol kg⁻¹ from ≈200 m water depth to the seafloor, respectively. In contrast, the Indian and North Pacific Oceans. These negative anomalies in Ba* appear to be associated with Circumpolar Deep Water and, below that, Antarctic Bottom Water; the influence of the latter can also be seen in near-bottom negative Ba* in the South Pacific, southern Indian, and South Atlantic Oceans (Fig. 8C). As with the other basins, the origin of the negative Ba* waters in the Southern Ocean likely reflects a combination of *in situ* and circulation-related phenomena. For example, in the Southern Ocean, Si is only stripped at the very surface, whereas particulate Ba formation is thought to be greatest in the mesopelagic (i.e., between 200–1,000 m; e.g., Stroobants et al. 1991). Barite formation is generally considered to be related to the regeneration of particulate organic matter (e.g., Chow & Goldberg, 1960), whereby the former consumes Ba and the latter releases Si. Thus, intense organic matter remineralization and associated pelagic BaSO₄ precipitation could contribute to negative Ba* in the mesopelagic Southern Ocean. Similarly, the Si cycle in the Southern Ocean tends to ‘trap’ a significant fraction of the global Si inventory in the waters circulating close to Antarctica (e.g., Holzer et al., 2014). Since the calculation of Ba* depends on both [Ba] and [Si], waters with elevated [Si] will exhibit positive Ba* around 2,000 m, between +5 and +15 nmol kg⁻¹ (Fig. 6). The most positive Ba* values, between +20 and +30 nmol kg⁻¹, are observed at lower Ba* whether or not there is elevated Ba removal.

By 2,000 m, almost all of the ocean north of 50 °S exhibits positive Ba* (Fig. 7C). By 4,000 m in the Pacific, specifically in the, the areal extent of the positive-Ba* waters shrinks to encompass

the area north of 30 °S (Fig. 8C). Despite covering a smaller area, the abyssal ocean exhibits the most positive Ba* values outside of the surface of the Southern Ocean. The reasons for elevated and increasing Ba* between the deep and abyssal oceans likely reflects a mixture of local and regional processes, and we offer two speculative explanations for these patterns. First, Si trapping in the Southern Ocean potentially renders most of the deep ocean away from Antarctica deficient in Si relative to Ba. Thus, much of the ocean may exhibit more positive Ba* than the deep circum-Antarctic region due to processes unrelated to Ba cycling. Second, the most positive Ba* values are generally found close to the seafloor, rather than the mid-depths, especially in the North Pacific, the Peru and Chile Basins ~~as well as~~, and the Philippine Sea (Fig. 7). ~~Vertical profiles of Ω_{barite} are~~. This may indicate a mechanism that preferentially removes Ba (relative to Si) from the mid-depths, or input of Ba (relative to Si) close to the seafloor.

Systematic variations in Ba* arise due to differences in the marine biogeochemical cycles of Ba and Si. While, in some cases, the specific drivers of these variations remains unresolved, our model identifies multiple hotspots of Ba–Si decoupling that warrant additional study.

5.3.3. Barite saturation state of seawater

Here we show that our approach can predict Ω_{barite} with an MAE of 0.08, that our output is in agreement with published values; ~~comparisons are provided in the Appendix~~, and that the deep ocean, below 1,000 m, is at saturation with respect to BaSO₄. By comparison to literature data, we estimate that our model achieves a typical prediction uncertainty on Ω_{barite} of 0.08 (see Appendix). Accordingly, values of Ω_{barite} between 0.92–1.08 can be considered as ‘BaSO₄ saturated,’ whereas values of $\Omega_{\text{barite}} < 0.92$ or > 1.08 indicate under- or super-saturation, respectively. Global patterns in Ω_{barite} derived using our model are similar to those reported by ~~(e.g., Jeandel et al., 1996; Monnin et al., (1999);) and~~ Rushdi et al., (2000). ~~Excepting the~~ Readers looking for detailed basin-by-basin descriptions of Ω_{barite} are directed to those studies. Briefly our model shows that, ~~excepting the~~ high latitudes, the surface ocean is undersaturated with respect to BaSO₄ (i.e., $\Omega_{\text{barite}} < 1$) ~~and the 0.92~~). The lowest values of Ω_{barite} in the open ocean are observed in the hot, salty cores of the Subtropical Gyres (Ω_{barite} between 0.1–0.2; ~~Figs. 4D, 8D~~). ~~Whereas~~ Fig. 5D). Conversely, the cold and fresh polar regions exhibit supersaturation at the sea surface, though there are important

differences between the Southern and Arctic Oceans. The Southern Ocean ~~remains supersaturated~~ (i.e., $\Omega_{\text{barite}} > 1$) exhibits BaSO_4 saturation to depths around 2,000 m, whereas the Arctic Ocean switches to undersaturated conditions below ~~the halocline (~250 m)~~. At 1,000 m, most of the North Pacific ~~is supersaturated~~ achieves saturation (or slight supersaturation) with respect to BaSO_4 (Fig. 6D) and ~~by~~ at 2,000 m almost all of the ocean exhibits $\Omega_{\text{barite}} > 1$, ~~excepting~~ 0.92. The main exceptions to this are the Atlantic Ocean, which is undersaturated at all depths, and the southern Indian Ocean between 35–50 °S (Fig. 6D7D). The South Pacific and Indian Oceans return to undersaturated conditions by 4,000 m, whereas ~~the majority parts~~ of the North Pacific ~~exhibits~~ $\Omega_{\text{barite}} > 1$ remain saturated to the seafloor (Fig. 7D8D). From a volumetric global perspective, the oceans are slightly undersaturated with respect to BaSO_4 : volume-weighted mean $\Omega_{\text{barite}} = 0.82$; however, the ocean ~~below~~ between 1,000–5,500 m exhibits a mean $\Omega_{\text{barite}} \geq 0.92$, ~~which~~ (Fig. 9). This result implies that ~~much of~~ the deep ocean, ~~as a whole~~, is close to ~~saturation~~ chemical equilibrium with respect to BaSO_4 (Fig. 8D).

5.3.4. Model applications ~~Lastly, in~~

In the spirit of maximizing model utility, we suggest three possible uses for ~~these data~~ model #3080 ~~outputs~~. First, the outputs can be used for model intercomparison and intercalibration. For example, a number of statistical models, such as Optimum Multiparameter Optimization, have been successfully used to study Ba cycling in the North Atlantic (Le Roy et al., 2018; Rahman et al., 2022), Southeast Pacific (Rahman et al., 2022), and Mediterranean Sea (Jullion et al., 2017). These models can apportion the relative contributions of *in situ* biogeochemical cycling and conservative mixing to observed [Ba]; however, accurate quantification of these processes requires *a priori* knowledge of end-member water mass [Ba], which model #33363080 can provide. Our model could also be used to benchmark output from process-based models, such as ~~the~~ Ocean Circulation Inverse ~~Model~~ Models (e.g., John et al., 2020; Roshan & DeVries, 2021). Second, the output can be used for interpolation purposes. ~~For example, many~~ Many groups investigated Ba partitioning into various types of marine carbonates (see Sect. 1 for examples); however, these investigations are sometimes performed without a co-located measurement of [Ba]. In these cases output from model #33363080 could be used to help calibrate specific substrates, such as deep-sea corals or benthic forams. This also avoids the potential for circular reasoning whereby [Si] is used

to estimate [Ba], which is then reconstructed from the Ba:Ca ratio of carbonates to estimate [Si]. Third, the model output makes testable predictions for regions of the ocean that have yet to be sampled by GEOTRACES-style surveys. Several of these regions, such as the Southern Ocean, exhibit with sharp lateral and vertical gradients in [Ba], Ba*, and Ω_{barite} . Such gradients should be considered prime targets for future process-oriented studies of marine Ba cycling.

6. Data availability

Data described in this manuscript can be accessed at the *Biological and Chemical Oceanography Data Management Office* under data doi:10.26008/1912/bco-dmo.885506.12 (Horner & Mete, 2023).

7. Conclusions

This study presents a spatially and vertically resolved global model of [Ba] determined using Gaussian Process Regression machine learning. The model reproduces several known features of the marine [Ba] distribution and makes testable predictions in regions that are yet to be sampled. Analysis of the model output reveals the mean oceanic [Ba] is 89 nmol kg⁻¹, implying a total marine Ba inventory of 122±87 Tmol. Using predictors from the World Ocean Atlas, we also estimate the global distribution of Ba* and Ω_{barite} . Both properties exhibit significant gradients that can be systematically investigated in future studies. The mean oceanic Ω_{barite} is 0.82, though between 1,000–5,500 m the mean is ≥ 0.92 , implying that the deep ocean is ~~close to saturation~~ at equilibrium with respect to BaSO₄. Our model output should prove valuable in studies of Ba biogeochemistry, specifically for statistical- and process-based model validation, calibrating sedimentary archives, and for identifying promising regions for further study. More broadly, our study demonstrates the utility of using machine learning to accurately simulate the distributions of trace elements in seawater. With minor adjustments, our approach could be employed to make predictions for other dissolved tracers in the sea.

Appendix

Here we compare our results with published profiles of Ω_{barite} . Our results were calculated using the thermodynamic model of Rusdi et al. (2000), model #33363080 [Ba], and WOA T , S , and pressure. Literature profiles of Ω_{barite} were calculated using one of three different thermodynamic models and *in situ* observations of [Ba], T , S , and pressure. In general, there is strong agreement between modeled and *in situ* Ω_{barite} whereby our model reproduces the shape of published profiles (Fig. A1). There are, however, some small systematic offsets between the various approaches, and we suspect that these derive from differences in the underlying thermodynamic models.

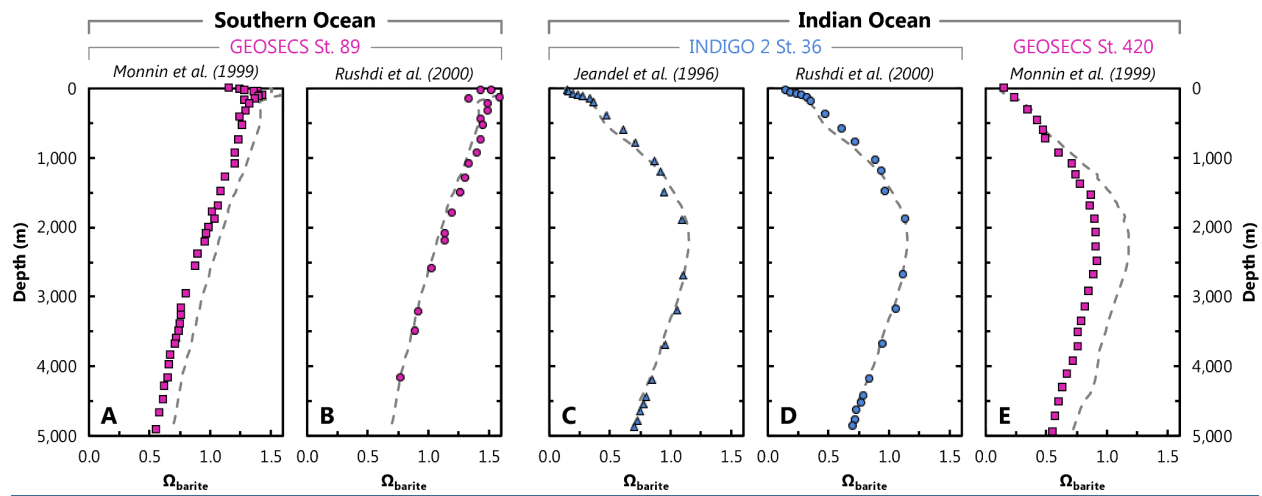


Figure A1. Comparison of literature- (symbols) and Model #33363080-derived (dashed line) estimates values of Ω_{barite} . Panels A and B show profiles of Ω_{barite} at GEOSECS St. 89 (60°0' S, 0°2' E). The other panels are from the Indian Ocean; C and D are from INDIGO 2 St. 36 (6°9' S, 50°55' E) and E from GEOSECS St. 420 (0°3' S, 50°55' E), some \approx 675 km north of INDIGO 2 St. 36.

We compare our model output with literature data Ω_{barite} at two stations locations in two basins (Fig. A1). These stations locations were selected for comparing Ω_{barite} because chosen to ensure a fair comparison between studies; at both locations each location, at least two studies calculated profiles of Ω_{barite} using the same underlying *in situ* data for [Ba], T , S , and pressure. This ensures a fair comparison between studies, since Thus, any differences in modeled Ω_{barite} should derive from the thermodynamic model and not the input data. Likewise, ~~the~~ literature profiles at these locations were based on calculations for pure, rather than strontian, BaSO_4 , as in our study. Published profiles of Ω_{barite} were extracted graphically from each study using *WebPlotDigitizer*

(Rohatgi, 2022). This extraction process may introduce some minor scatter in the literature data, though this is relatively minor ~~relative~~compared to the range of variation in Ω_{barite} .

First, we examine profiles of Ω_{barite} reported for GEOSECS St. 89 in the Southern Ocean (Fig. A1; Monnin et al., 1999; Rushdi et al., 2000). Modeled and published profiles show supersaturation in the surface ocean and undersaturation below 2,000–2,500 m. Profiles from Rushdi et al. (2000) show excellent agreement with Ω_{barite} calculated from model #~~3336~~3080 [Ba] and WOA T , S , and pressure, with our output ~~slightly negatively~~ offset by a MADMAE of 0.06 ($n = 22$). Given that we use the same thermodynamic model as Rushdi et al. (2000), the overall excellent agreement with their study is not surprising. However, the result is nonetheless reassuring since our study uses mean annual values for the various inputs, whereas Rushdi et al. (2000) utilized *in situ* data. There is a slightly larger offset between our profile of Ω_{barite} and that calculated by Monnin et al. (1999), with our respective profile ~~offset to higher Ω_{barite} by a MAD~~exhibiting an MAE of 0.13 ($n = 41$). This most likely reflects differences in the underlying thermodynamic model and not the *in situ* data since our model reproduces the same overall profile shape as Monnin et al. (1999). Likewise, both Monnin et al. (1999) and Rushdi et al. (2000) used the same *in situ* input data and their results are highly comparable, albeit with an offset similar to that between our results and Monnin et al. (1999).

Next we examine profiles of Ω_{barite} in the Indian Ocean for samples from INDIGO 2 St. 36 (Fig. A1; Jeandel et al., 1996; Rushdi et al., 2000). Profiles of Ω_{barite} show undersaturation at the surface, moderate supersaturation between 2,000–3,500 m, then return to undersaturated conditions down to the seafloor. Our profile shows overall excellent agreement with that of Jeandel et al. (1996), whereby ~~our data are offset to slightly lower a comparison of Ω_{barite} with~~yields a MADMAE of of 0.0603 ($n = 21$). ~~The largest differences are observed between 594–1,042 m depth, where the MAD is 0.15 ($n = 3$).~~ Our profile shows similarly good agreement with ~~that of~~ Rushdi et al. (2000), whereby ~~our data are offset to lower a comparison between our respective values of Ω_{barite} with~~yields a MADMAE of 0.0704 ($n = 20$). ~~As with the data of Jeandel et al. (1996), we observe a larger offset between modeled Ω_{barite} and the data of Rushdi et al. (2000) between 594–1,042 m, equivalent to a MAD of 0.17 ($n = 3$). We consider these larger mesopelagic offsets in Ω_{barite} to be the result of differences in the predictors (i.e., [Ba], T , S), rather than the thermodynamic model;~~

~~Jeandel et al. (1996) and Rushdi et al. (2000) use the same *in situ* predictor data and yield similar Ω_{barite} , despite using different thermodynamic models.~~

We also compared our results with data from St. 420 of GEOSECS (Monnin et al., 1999), which is located ≈ 675 km north of INDIGO 2 St. 36 (Fig. 2). As with data from the Southern Ocean (GEOSECS St. 89), our profile data are offset to higher Ω_{barite} than those of Monnin et al. (1999) ~~by a MAD~~, with slightly larger MAE of 0.1216 ($n = 29$). However, our modeled Ω_{barite} is generally in much closer agreement with Monnin et al. (1999) above 1,250100 m than below, equivalent to a ~~MAD~~MAE of 0.0304 ($n = 98$) and 0.1621 ($n = 2021$), respectively. In this case it is more challenging to ascribe a unique cause of the differences in calculated Ω_{barite} ; these offsets could relate to differences in the predictors or the thermodynamic model.

We can use these comparisons to estimate the prediction uncertainty on our model-derived values of Ω_{barite} . The MAE of the 133 comparisons shown in Fig. A1 yields a value of 0.10. However, there are different numbers of points in each profile; we thus believe it is more appropriate to average the MAE calculated for each of the five profiles, which yields a value of 0.08. Both values are similar to the 10 % prediction uncertainty reported by Monnin et al. (1999).

Overall, our ML-derived profiles of Ω_{barite} show excellent agreement with *in situ* data, both in terms of profile shape and ~~absolute~~-values of Ω_{barite} . We use this comparison to ~~within~~estimate the prediction uncertainty on ML-derived values of Ω_{barite} , which we calculate as being between 0.108 and 0.10. Should a revised thermodynamic model and/or improved BaSO_4 solubility coefficients become available, a new grid of Ω_{barite} could be calculated using Model #~~3336~~3080 [Ba] and WOA T , S , and pressure data.

Author contributions

Project conceptualization and funding acquisition by T.J.H. Data curation, formal analysis, investigation, and methodology by O.Z.M., A.V.S., [H.H.K.](#), and T.J.H. Data visualization by A.V.S. and T.J.H. Software provided by O.Z.M., A.V.S., H.H.K., and A.G.D. Writing (original draft) by O.Z.M. and T.J.H.; review and editing by [A.V.S.](#), H.H.K., A.G.D., L.M.W., A.M.S., M.G., and W.D.L.

Competing interests

The authors declare that they have no conflict of interest.

Acknowledgements

We are thankful to the many data originators who contributed ~~—and the funding agencies that enabled the generation of—quality controlled~~ dissolved Ba data to the 2021 GEOTRACES Intermediate Data Product, [as well as the funding agencies that made those contributions possible](#). The GEOTRACES IDP represents an international collaboration and is endorsed by the Scientific Committee on Oceanic Research. We are especially grateful to Frank Dehairs, who provided comments on an early draft of the text and shared additional testing data from the Indian Ocean, as well as Karen Grissom, who provided laboratory assistance to A.M.S. We kindly acknowledge use of the *Discovery* high-performance compute nodes at Dartmouth College Research Computing. [We are grateful to the Editor, Christophe Monnin, Frank Pavia, and two anonymous reviewers who provided insightful and constructive comments that helped us improve the study.](#)

Financial support

O.Z.M was supported by WHOI's Academic Programs Office through a *Summer Student Fellowship*. A.M.S. acknowledges support from the U.S. National Science Foundation (OCE-0927951, OCE-1137851, OCE-1261214, OCE-1436312, and OCE-1737024), as does T.J.H. (OCE-1736949 and OCE-2023456). T.J.H. was further supported by *The Andrew W. Mellon Foundation Endowed Fund for Innovative Research* and *The Breene M. Kerr Early Career Scientist Endowment Fund*.

References

- Anagnostou, E., Sherrell, R. M., Gagnon, A., LaVigne, M., Field, M. P., & McDonough, W. F. (2011). Seawater nutrient and carbonate ion concentrations recorded as P/Ca, Ba/Ca, and U/Ca in the deep-sea coral *Desmophyllum dianthus*. *Geochimica et Cosmochimica Acta*, 75(9), 2529–2543. <https://doi.org/10.1016/j.gca.2011.02.019>
- Ancombe, F. J. (1973). Graphs in Statistical Analysis. *The American Statistician*, 27(1), 17-21. <https://doi.org/10.1080/00031305.1973.10478966>
- [Baars, O., Abouchami, W., Galer, S. J., Boye, M., & Croot, P. L. \(2014\). Dissolved cadmium in the Southern Ocean: Distribution, speciation, and relation to phosphate. *Limnology and Oceanography*, 59\(2\), 385-399. <https://doi.org/10.4319/lo.2014.59.2.0385>](#)
- Bains, S., Norris, R. D., Corfield, R. M., & Faul, K. L. (2000). Termination of global warmth at the Palaeocene/Eocene boundary through productivity feedback. *Nature*, 407(6801), 171–174. <https://doi.org/10.1038/35025035>
- Bates, S. L., Hendry, K. R., Pryer, H. V., Kinsley, C. W., Pyle, K. M., Woodward, E. M. S., & Horner, T. J. (2017). Barium isotopes reveal role of ocean circulation on barium cycling in the Atlantic. *Geochimica et Cosmochimica Acta*, 204, 286–299. <https://doi.org/10.1016/j.gca.2017.01.043>
- Boyer, Tim P.; García, Hernán E.; Locarnini, Ricardo A.; Zweng, Melissa M.; Mishonov, Alexey V.; Reagan, James R.; Weathers, Katharine A.; Baranova, Olga K.; Paver, Christopher R.; Seidov, Dan; Smolyar, Igor V. (2018). World Ocean Atlas 2018. NOAA National Centers for Environmental Information. Dataset. <https://www.ncei.noaa.gov/archive/accession/NCEI-WOA18>
- Bishop, J. K. (1988). The barite–opal–organic carbon association in oceanic particulate matter. *Nature*, 332(6162), 341-343.
- [Bishop, J. K. B. \(1988\). Regional extremes in particulate matter composition and flux: Effects on the chemistry of the ocean interior. In Berger, W. H., Smetacek, V. S., and Wefer, G. \(Eds.\) *Productivity of the Ocean. Present and Past*, 117-137. Wiley-Interscience.](#)
- Blount, C. W. (1977). Barite solubilities and thermodynamic quantities up to 300 degrees C and 1400 bars. *American Mineralogist*, 62(9–10), 942–957.
- Boyle, E., & Edmond, J. M. (1975). Copper in surface waters south of New Zealand. *Nature*, 253(5487), 107–109. <https://doi.org/10.1038/253107a0>
- Bridgestock, L., Hsieh, Y.-T., Porcelli, D., Homoky, W. B., Bryan, A., & Henderson, G. M. (2018). Controls on the barium isotope compositions of marine sediments. *Earth and Planetary Science Letters*, 481, 101–110. <https://doi.org/10.1016/j.epsl.2017.10.019>
- Cao, Z., Li, Y., Rao, X., Yu, Y., Hathorne, E. C., Siebert, C., Dai, M., & Frank, M. (2020). Constraining barium isotope fractionation in the upper water column of the South China Sea. *Geochimica et Cosmochimica Acta*, 288, 120–137. <https://doi.org/10.1016/j.gca.2020.08.008>

- [Cao, Z., Rao, X., Yu, Y., Siebert, C., Hathorne, E. C., Liu, B., et al. \(2021\). Stable barium isotope dynamics during estuarine mixing. *Geophysical Research Letters*, **48**\(19\), e2021GL095680. <https://doi.org/10.1029/2021GL095680>.](https://doi.org/10.1029/2021GL095680)
- Carter, S. C., Paytan, A., & Griffith, E. M. (2020). Toward an Improved Understanding of the Marine Barium Cycle and the Application of Marine Barite as a Paleoproductivity Proxy. *Minerals*, *10*(5), 421. <https://doi.org/10.3390/min10050421>
- Chan, L. H., Drummond, D., Edmond, J. M., & Grant, B. (1977). On the barium data from the Atlantic GEOSECS expedition. *Deep Sea Research*, *24*(7), 613–649. [https://doi.org/10.1016/0146-6291\(77\)90505-7](https://doi.org/10.1016/0146-6291(77)90505-7) [https://doi.org/10.1016/0146-6291\(77\)90505-7](https://doi.org/10.1016/0146-6291(77)90505-7).
- [Charbonnier, Q., Bouchez, J., Gaillardet, J., & Gayer, É. \(2020\). Barium stable isotopes as a fingerprint of biological cycling in the Amazon River basin. *Biogeosciences*, **17**\(23\), 5989-6015. <https://doi.org/10.5194/bg-17-5989-2020>.](https://doi.org/10.5194/bg-17-5989-2020)
- Chow, T. J., & Goldberg, E. D. (1960). On the marine geochemistry of barium. *Geochimica et Cosmochimica Acta*, *20*(3), 192–198. [https://doi.org/10.1016/0016-7037\(60\)90073-9](https://doi.org/10.1016/0016-7037(60)90073-9)
- Coffey, M., Dehairs, F., Collette, O., Luther, G., Church, T., & Jickells, T. (1997). The Behaviour of Dissolved Barium in Estuaries. *Estuarine, Coastal and Shelf Science*, **45**(1), 113–121. <https://doi.org/10.1006/ecss.1996.0157>
- Copernicus Marine Environment Monitoring Service. (2021). *Global Ocean Chlorophyll, PP and PFT (Copernicus-GlobColour) from Satellite Observations: Monthly and Daily Interpolated (Reprocessed from 1997)* [Data set]. Mercator Ocean International. <https://doi.org/10.48670/MOI-00100>
- Craig, H., & Turekian, K. K. (1980). The GEOSECS program: 1976-1979. *Earth and Planetary Science Letters*, **49**(2), 263-265. [https://doi.org/10.1016/0012-821X\(76\)90062-5](https://doi.org/10.1016/0012-821X(76)90062-5).
- Crameri, F. (2018). Scientific colour maps. *Zenodo*. <https://doi.org/10.5281/zenodo.5501399>.
- [Cressie, N.A.C. \(1993\). Spatial Prediction and Kriging. In *Statistics for Spatial Data*, N.A.C. Cressie \(Ed.\). <https://doi.org/10.1002/9781119115151.ch3>.](https://doi.org/10.1002/9781119115151.ch3)
- Crockford, P. W., Wing, B. A., Paytan, A., Hodgskiss, M. S. W., Mayfield, K. K., Hayles, J. A., Middleton, J. E., Ahm, A.-S. C., Johnston, D. T., Caxito, F., Uhlein, G., Halverson, G. P., Eickmann, B., Torres, M., & Horner, T. J. (2019). Barium-isotopic constraints on the origin of post-Marinoan barites. *Earth and Planetary Science Letters*, *519*, 234–244. <https://doi.org/10.1016/j.epsl.2019.05.018>.
- Cutter, G. A. (2013). Intercalibration in chemical oceanography—getting the right number. *Limnology and Oceanography: Methods*, **11**(7), 418-424.
- Dehairs, F., Chesselet, R., & Jedwab, J. (1980). Discrete suspended particles of barite and the barium cycle in the open ocean. *Earth and Planetary Science Letters*, *49*(2), 528–550. [https://doi.org/10.1016/0012-821X\(80\)90094-1](https://doi.org/10.1016/0012-821X(80)90094-1)

- DeVries, T. (2014). The oceanic anthropogenic CO₂ sink: Storage, air-sea fluxes, and transports over the industrial era. *Global Biogeochemical Cycles*, 28(7), 631-647. <https://doi.org/10.1002/2013GB004739>
- Dickens, G. R., Fewless, T., Thomas, E., & Bralower, T. J. (2003). Excess barite accumulation during the Paleocene-Eocene thermal Maximum: Massive input of dissolved barium from seafloor gas hydrate reservoirs. In S. L. Wing, P. D. Gingerich, B. Schmitz, & E. Thomas, *Causes and consequences of globally warm climates in the early Paleogene*. Geological Society of America. <https://doi.org/10.1130/0-8137-2369-8.11>
- Dymond, J., Suess, E., & Lyle, M. (1992). Barium in Deep-Sea Sediment: A Geochemical Proxy for Paleoproductivity. *Paleoceanography*, 7(2), 163-181. <https://doi.org/10.1029/92PA00181>.
- Eagle, M., Paytan, A., Arrigo, K. R., van Dijken, G., & Murray, R. W. (2003). A comparison between excess barium and barite as indicators of carbon export. *Paleoceanography*, 18(1). <https://doi.org/10.1029/2002PA000793>
- Eakins, B.W., & Sharman, G.F. (2010). Volumes of the World's Oceans from ETOPO1. *NOAA National Geophysical Data Center, Boulder, CO*. https://www.ngdc.noaa.gov/mgg/global/etopo1_ocean_volumes.html
- Edmond, J. M., Boyle, E. D., Drummond, D., Grant, B., & Mislick, T. (1978). Desorption of barium in the plume of the Zaire (Congo) River. *Netherlands Journal of Sea Research*, (3-4).
- Esser, B. K., & Volpe, A. M. (2002). At-sea high-resolution chemical mapping: Extreme barium depletion in North Pacific surface water. *Marine Chemistry*, 79(2), 67-79. [https://doi.org/10.1016/S0304-4203\(02\)00037-3](https://doi.org/10.1016/S0304-4203(02)00037-3)
- García H. E., K.W. Weathers, C.R. Paver, I. Smolyar, T.P. Boyer, R.A. Locarnini, M.M. Zweng, A.V. Mishonov, O.K. Baranova, D. Seidov, and J.R. Reagan (2018a). World Ocean Atlas 2018, Volume 3: Dissolved Oxygen, Apparent Oxygen Utilization, and Dissolved Oxygen Saturation. A. Mishonov Technical Editor. NOAA Atlas NESDIS 83, 38pp. <http://www.nodc.noaa.gov/OC5/indprod.html>
- García H.E., K.W. Weathers, C.R. Paver, I. Smolyar, T.P. Boyer, R.A. Locarnini, M.M. Zweng, A.V. Mishonov, O.K. Baranova, D. Seidov, and J.R. Reagan (2018b). World Ocean Atlas 2018. Vol. 4: Dissolved Inorganic Nutrients (phosphate, nitrate and nitrate+nitrite, silicate). A. Mishonov Technical Editor, NOAA Atlas NESDIS 84, 35pp. <http://www.nodc.noaa.gov/OC5/indprod.html>
- GEOTRACES Intermediate Data Product Group (2021). The GEOTRACES Intermediate Data Product 2021 (IDP2021). NERC EDS British Oceanographic Data Centre NOC. doi:10.5285/cf2d9ba9-d51d-3b7c-e053-8486abc0f5fd.
- Glover, D., Jenkins, W., & Doney, S. (2011). *Modeling Methods for Marine Science*. Cambridge: Cambridge University Press. doi:10.1017/CBO9780511975721

Gonneea, M. E., Cohen, A. L., DeCarlo, T. M., & Charette, M. A. (2017). Relationship between water and aragonite barium concentrations in aquaria reared juvenile corals. *Geochimica et Cosmochimica Acta*, 209, 123-134.

Griffith, E. M., Fantle, M. S., Eisenhauer, A., Paytan, A., & Bullen, T. D. (2015). Effects of ocean acidification on the marine calcium isotope record at the Paleocene–Eocene Thermal Maximum. *Earth and Planetary Science Letters*, 419, 81–92. <https://doi.org/10.1016/j.epsl.2015.03.010>

Gruber, N., & Sarmiento, J. L. (1997). Global patterns of marine nitrogen fixation and denitrification. *Global Biogeochemical Cycles*, 11(2), 235-266. <https://doi.org/10.1029/97GB00077>

Guay, C. K., & Falkner, K. K. (1998). A survey of dissolved barium in the estuaries of major Arctic rivers and adjacent seas. *Continental Shelf Research*, 18(8), 859-882. [https://doi.org/10.1016/S0278-4343\(98\)00023-5](https://doi.org/10.1016/S0278-4343(98)00023-5)

Hathorne, E. C., Gagnon, A., Felis, T., Adkins, J., Asami, R., Boer, W., Caillon, N., Case, D., Cobb, K. M., Douville, E., deMenocal, P., Eisenhauer, A., Garbe-Schönberg, D., Geibert, W., Goldstein, S., Hughen, K., Inoue, M., Kawahata, H., Kölling, M., Cornec, F. L., Linsley, B. K., McGregor, H. V., Montagna, P., Nurhati, I. S., Quinn, T. M., Raddatz, J., Rebaubier, H., Robinson, L., Sadekov, A., Sherrell, R., Sinclair, D., Tudhope, A. W., Wei, G., Wong, H., Wu, H. C., You, C.-F. (2013). Interlaboratory study for coral Sr/Ca and other element/Ca ratio measurements. *Geochemistry, Geophysics, Geosystems*, 14(9), 3730–3750. <https://doi.org/10.1002/ggge.20230>

Hayes, C. T., Anderson, R. F., Cheng, H., Conway, T. M., Edwards, R. L., Fleisher, M. Q., Ho, P., Huang, K.-F., John, S. G., Landing, W. M., Little, S. H., Lu, Y., Morton, P. L., Moran, S. B., Robinson, L. F., Shelley, R. U., Shiller, A. M., & Zheng, X.-Y. (2018). Replacement Times of a Spectrum of Elements in the North Atlantic Based on Thorium Supply. *Global Biogeochemical Cycles*, 32(9), 1294–1311. <https://doi.org/10.1029/2017GB005839>

Hayes, C. T., Costa, K. M., Anderson, R. F., Calvo, E., Chase, Z., Demina, L. L., Dutay, J.-C., German, C. R., Heimbürger-Boavida, L.-E., Jaccard, S. L., Jacobel, A., Kohfeld, K. E., Kravchishina, M. D., Lippold, J., Mekik, F., Missiaen, L., Pavia, F. J., Paytan, A., Pedrosa-Pamies, R., Petrova, M. V., Rahman, S., Robinson, L. F., Roy-Barman, M., Sanchez-Vidal, A., Shiller, A., Tagliabue, A., Tessin, A. C., van Hulten, M., Zhang, J. (2021). Global Ocean Sediment Composition and Burial Flux in the Deep Sea. *Global Biogeochemical Cycles*, 35(4), e2020GB006769. <https://doi.org/10.1029/2020GB006769>

Holte, J., Talley, L. D., Gilson, J., & Roemmich, D. (2017). An Argo mixed layer climatology and database. *Geophysical Research Letters*, 44(11), 5618–5626. <https://doi.org/10.1002/2017GL073426> <https://doi.org/10.1002/2017GL073426>

Holzer, M., Primeau, F. W., DeVries, T., & Matear, R. (2014). The Southern Ocean silicon trap: Data-constrained estimates of regenerated silicic acid, trapping efficiencies, and global transport paths. *Journal of Geophysical Research: Oceans*, 119(1), 313-331. <https://doi.org/10.1002/2013JC009356>

- Hood, E.M., C.L. Sabine, and B.M. Sloyan, eds. (2010). The GO-SHIP Repeat Hydrography Manual: A Collection of Expert Reports and Guidelines. *IOCCP Report Number 14*, ICPO Publication Series Number 134. Available online at <http://www.go-ship.org/HydroMan.html>.
- Hönisch, B., Allen, K. A., Russell, A. D., Eggins, S. M., Bijma, J., Spero, H. J., Lea, D. W., & Yu, J. (2011). Planktic foraminifers as recorders of seawater Ba/Ca. *Marine Micropaleontology*, 79(1–2), 52–57. <https://doi.org/10.1016/j.marmicro.2011.01.003>
- Hoppema, M., Dehairs, F., Navez, J., Monnin, C., Jeandel, C., Fahrbach, E., & de Baar, H. J. W. (2010). Distribution of barium in the Weddell Gyre: Impact of circulation and biogeochemical processes. *Marine Chemistry*, 122(1), 118–129. <https://doi.org/10.1016/j.marchem.2010.07.005>
- ~~Horner, T. J., Kinsley, C. W., & Nielsen, S. G. (2015). Barium-isotopic fractionation in seawater mediated by barite cycling and oceanic circulation. *Earth and Planetary Science Letters*, 430, 511–522. <https://doi.org/10.1016/j.epsl.2015.07.027>~~
- Horner, T. J., & Crockford, P. W. (2021). *Barium Isotopes: Drivers, Dependencies, and Distributions through Space and Time* (1st ed.). Cambridge University Press. <https://doi.org/10.1017/9781108865845>.
- ~~Horner, T. J., Kinsley, C. W., & Nielsen, S. G. (2015). Barium isotopic fractionation in seawater mediated by barite cycling and oceanic circulation. *Earth and Planetary Science Letters*, 430, 511–522. <https://doi.org/10.1016/j.epsl.2015.07.027>~~
- ~~Hsieh, Y.-T., & Henderson, G. M. (2017). Barium stable isotopes in the global ocean: Tracer of Ba inputs and utilization. *Earth and Planetary Science Letters*, 473, 269–278. <https://doi.org/10.1016/j.epsl.2017.06.024>~~
- ~~Horner, T. J., Mete, O. Z. (2023) A spatially and vertically resolved global grid of dissolved barium concentrations in seawater determined using Gaussian Process Regression machine learning. [Data Set]. *Biological and Chemical Oceanography Data Management Office* (BCO-DMO). (Version 1) Version Date 2023-02-22. <https://www.bco-dmo.org/dataset/885506>; doi:10.26008/1912/bco-dmo.885506.1.~~
- Hsieh, Y.-T., & Henderson, G. M. (2017). Barium stable isotopes in the global ocean: Tracer of Ba inputs and utilization. *Earth and Planetary Science Letters*, 473, 269–278. <https://doi.org/10.1016/j.epsl.2017.06.024>
- Jacquet, S. H. M., Dehairs, F., & Rintoul, S. (2004). A high resolution transect of dissolved barium in the Southern Ocean. *Geophysical Research Letters*, 31(14). <https://doi.org/10.1029/2004GL020016>
- Jeandel, C., Dupré, B., Lebaron, G., Monnin, C., & Minster, J.-F. (1996). Longitudinal distributions of dissolved barium, silica and alkalinity in the western and southern Indian Ocean. *Deep Sea Research Part I: Oceanographic Research Papers*, 43(1), 1–31. [https://doi.org/10.1016/0967-0637\(95\)00098-4](https://doi.org/10.1016/0967-0637(95)00098-4)

- John, S. G., Liang, H., Weber, T., DeVries, T., Primeau, F., Moore, K., Holzer, M., Mahowald, N., Gardner, W., Mishonov, A., Richardson, M. J., Faugere, Y., & Taburet, G. (2020). AWESOME OCIM: A simple, flexible, and powerful tool for modeling elemental cycling in the oceans. *Chemical Geology*, 533, 119403. <https://doi.org/10.1016/j.chemgeo.2019.119403>
- Joung, D., & Shiller, A. M. (2014). Dissolved barium behavior in Louisiana Shelf waters affected by the Mississippi/Atchafalaya River mixing zone. *Geochimica et Cosmochimica Acta*, 141, 303–313. <https://doi.org/10.1016/j.gca.2014.06.021>
- Jullion, L., Jacquet, S. H. M., & Tanhua, T. (2017). Untangling biogeochemical processes from the impact of ocean circulation: First insight on the Mediterranean dissolved barium dynamics. *Global Biogeochemical Cycles*, 31(8), 1256–1270. <https://doi.org/10.1002/2016GB005489>
- Kawabe, M., & Fujio, S. (2010). Pacific Ocean circulation based on observation. *Journal of Oceanography*, 66, 389–403. <https://doi.org/10.1007/s10872-010-0034-8>
- Komagoe, T., Watanabe, T., Shirai, K., Yamazaki, A., & Uematu, M. (2018). Geochemical and Microstructural Signals in Giant Clam *Tridacna Maxima* Recorded Typhoon Events at Okinotori Island, Japan. *Journal of Geophysical Research: Biogeosciences*, 123(5), 1460–1474. <https://doi.org/10.1029/2017JG004082>
- LaVigne, M., Grottoli, A. G., Palardy, J. E., & Sherrell, R. M. (2016). Multi-colony calibrations of coral Ba/Ca with a contemporaneous in situ seawater barium record. *Geochimica et Cosmochimica Acta*, 179, 203–216. <https://doi.org/10.1016/j.gca.2015.12.038>
- LaVigne, M., Hill, T. M., Spero, H. J., & Guilderson, T. P. (2011). Bamboo coral Ba/Ca: Calibration of a new deep ocean refractory nutrient proxy. *Earth and Planetary Science Letters*, 312(3), 506–515. <https://doi.org/10.1016/j.epsl.2011.10.013>
- Lea, D. W., & Boyle, E. A. (1990). Foraminiferal reconstruction of barium distributions in water masses of the glacial oceans. *Paleoceanography*, 5(5), 719–742. <https://doi.org/10.1029/PA005i005p00719>
- Lea, D. W., Shen, G. T., & Boyle, E. A. (1989). Coralline barium records temporal variability in equatorial Pacific upwelling. *Nature*, 340(6232), 373–376. <https://doi.org/10.1038/340373a0>
- Le Roy, E., Sanial, V., Charette, M. A., van Beek, P., Lacan, F., Jacquet, S. H. M., Henderson, P. B., Souhaut, M., García-Ibáñez, M. I., Jeandel, C., Pérez, F. F., & Sarthou, G. (2018). The ²²⁶Ra–Ba relationship in the North Atlantic during GEOTRACES-GA01. *Biogeosciences*, 15(9), 3027–3048. <https://doi.org/10.5194/bg-15-3027-2018>
- Light, T., & Norris, R. (2021). Quantitative visual analysis of marine barite microcrystals: Insights into precipitation and dissolution dynamics. *Limnology and Oceanography*, 66(10), 3619–3629. <https://doi.org/10.1002/lno.11902>
- Locarnini, R.A., A.V. Mishonov, O.K. Baranova, T.P. Boyer, M.M. Zweng, H.E. Garcia, J.R. Reagan, D. Seidov, K.W. Weathers, C.R. Paver, and I.V. Smolyar (2018). World Ocean Atlas

- 2018, Volume 1: Temperature. A. Mishonov, Technical Editor. NOAA Atlas NESDIS 81, 52pp. <https://www.nodc.noaa.gov/OC5/indprod.html> .
- Monnin, C., Jeandel, C., Cattaldo, T., & Dehairs, F. (1999). The marine barite saturation state of the world's oceans. *Marine Chemistry*, 65(3), 253–261. [https://doi.org/10.1016/S0304-4203\(99\)00016-X](https://doi.org/10.1016/S0304-4203(99)00016-X)
- National Geophysical Data Center (1993). 5-minute Gridded Global Relief Data (ETOPO5). National Geophysical Data Center, NOAA. <https://doi.org/10.7289/V5D798BF>.
- [Orsi, A. H., Whitworth III, T., & Nowlin Jr, W. D. \(1995\). On the meridional extent and fronts of the Antarctic Circumpolar Current. *Deep Sea Research Part I: Oceanographic Research Papers*, 42\(5\), 641-673. \[https://doi.org/10.1016/0967-0637\\(95\\)00021-W\]\(https://doi.org/10.1016/0967-0637\(95\)00021-W\)](#)
- Paytan, A., & Griffith, E. M. (2007). Marine barite: Recorder of variations in ocean export productivity. *Deep Sea Research Part II: Topical Studies in Oceanography*, 54(5), 687–705. <https://doi.org/10.1016/j.dsr2.2007.01.007>
- Paytan, A., Griffith, E. M., Eisenhauer, A., Hain, M. P., Wallmann, K., & Ridgwell, A. (2021). A 35-million-year record of seawater stable Sr isotopes reveals a fluctuating global carbon cycle. *Science*, 371(6536), 1346–1350. <https://doi.org/10.1126/science.aaz9266>
- Paytan, A., & Kastner, M. (1996). Benthic Ba fluxes in the central Equatorial Pacific, implications for the oceanic Ba cycle. *Earth and Planetary Science Letters*, 142(3), 439–450. [https://doi.org/10.1016/0012-821X\(96\)00120-3](https://doi.org/10.1016/0012-821X(96)00120-3)
- Paytan, A., Kastner, M., Campbell, D., & Thiemens, M. H. (1998). Sulfur Isotopic Composition of Cenozoic Seawater Sulfate. *Science*, 282(5393), 1459–1462. <https://doi.org/10.1126/science.282.5393.1459>
- Paytan, A., Kastner, M., Martin, E. E., Macdougall, J. D., & Herbert, T. (1993). Marine barite as a monitor of seawater strontium isotope composition. *Nature*, 366(6454), 445–449. <https://doi.org/10.1038/366445a0>
- Pyle, K. M., Hendry, K. R., Sherrell, R. M., Legge, O., Hind, A. J., Bakker, D., Venables, H., & Meredith, M. P. (2018). Oceanic fronts control the distribution of dissolved barium in the Southern Ocean. *Marine Chemistry*, 204, 95–106. <https://doi.org/10.1016/j.marchem.2018.07.002>
- Rafter, P. A., Bagnell, A., Marconi, D., & DeVries, T. (2019). Global trends in marine nitrate N isotopes from observations and a neural network-based climatology. *Biogeosciences*, 16(13), 2617–2633. <https://doi.org/10.5194/bg-16-2617-2019>
- Rahman, S., Shiller, A. M., Anderson, R. F., Charette, M. A., Hayes, C. T., Gilbert, M., Grissom, K. R., Lam, P. J., Ohnemus, D. C., Pavia, F. J., Twining, B. S., & Vivancos, S. M. (2022). Dissolved and particulate barium distributions along the US GEOTRACES North Atlantic and East Pacific Zonal Transects (GA03 and GP16): Global implications for the marine barium cycle. *Global Biogeochemical Cycles*, 36(6), e2022GB007330. <https://doi.org/10.1029/2022GB007330>.

- Raju, K., & Atkinson, G. (1988). Thermodynamics of “scale” mineral solubilities. 1. Barium sulfate(s) in water and aqueous sodium chloride. *Journal of Chemical & Engineering Data*, 33(4), 490–495. <https://doi.org/10.1021/je00054a029>
- Rasmussen, C. E., & Williams, C. K. I. (2006). *Gaussian processes for machine learning*. MIT Press.
- Roeske, T., Loeff, M. R. vd, Middag, R., & Bakker, K. (2012). Deep water circulation and composition in the Arctic Ocean by dissolved barium, aluminium and silicate. *Marine Chemistry*, 132–133, 56–67. <https://doi.org/10.1016/j.marchem.2012.02.001>.
- Rohatgi, A. (2022). WebPlotDigitizer. Version: 4.6, Pacifica, CA, USA. <https://automeris.io/WebPlotDigitizer>.
- Roshan, S., DeVries, T., Wu, J., & Chen, G. (2018). The internal cycling of zinc in the ocean. *Global biogeochemical cycles*, 32(12), 1833-1849.
- Roshan, S., DeVries, T., & Wu, J. (2020). Constraining the global ocean Cu cycle with a data-assimilated diagnostic model. *Global Biogeochemical Cycles*, 34(11), e2020GB006741.
- Roshan, S., & DeVries, T. (2021). Global Contrasts Between Oceanic Cycling of Cadmium and Phosphate. *Global Biogeochemical Cycles*, 35(6). <https://doi.org/10.1029/2021GB006952>
- Rushdi, A. I., McManus, J., & Collier, R. W. (2000). Marine barite and celestite saturation in seawater. *Marine Chemistry*, 69(1–2), 19–31. [https://doi.org/10.1016/S0304-4203\(99\)00089-4](https://doi.org/10.1016/S0304-4203(99)00089-4)
- Samanta, S., & Dalai, T. K. (2016). Dissolved and particulate Barium in the Ganga (Hooghly) River estuary, India: Solute-particle interactions and the enhanced dissolved flux to the oceans. *Geochimica et Cosmochimica Acta*, 195, 1–28. <https://doi.org/10.1016/j.gca.2016.09.005> <https://doi.org/10.1016/j.gca.2016.09.005>
- Sarmiento, J. L., Gruber, N., Brzezinski, M. A., & Dunne, J. P. (2004). High-latitude controls of thermocline nutrients and low latitude biological productivity. *Nature*, 427(6969), 56-60. <https://doi.org/10.1038/nature02127>
- Schenau, S. J., Prins, M. A., De Lange, G. J., & Monnin, C. (2001). Barium accumulation in the Arabian Sea: Controls on barite preservation in marine sediments. *Geochimica et Cosmochimica Acta*, 65(10), 1545–1556. [https://doi.org/10.1016/S0016-7037\(01\)00547-6](https://doi.org/10.1016/S0016-7037(01)00547-6).
- Schlitzer, R. (2023). Ocean Data View, <https://odv.awi.de>.
- Schlitzer, R., Anderson, R. F., Dodas, E. M., Lohan, M., Geibert, W., Tagliabue, A., Bowie, A., Jeandel, C., Maldonado, M. T., Landing, W. M., Cockwell, D., Abadie, C., Abouchami, W., Achterberg, E. P., Agather, A., Aguiar-Islas, A., van Aken, H. M., Andersen, M., Archer, C., Auro M., de Baar H. J., Baars O., Baker A. R., Bakker K., Basak C., Baskaran M., Bates N. R., Bauch D., van Beek P., Behrens M. K., Black E., Bluhm K., Bopp L., Bouman H., Bowman K., Bown J., Boyd P., Boye M., Boyle E. A., Branellec P., Bridgestock L., Brissebrat G., Browning T., Bruland K. W., Brumsack H.J., Brzezinski M., Buck C. S., Buck K. N., Buesseler K., Bull A., Butler E., Cai P., Mor P. C., Cardinal D., Carlson C., Carrasco G.,

Casacuberta N., Casciotti K. L., Castrillejo M., Chamizo E., Chance R., Charette M. A., Chaves J. E., Cheng H., Chever F., Christl M., Church T. M., Closset I., Colman A., Conway T. M., Cossa D., Croot P., Cullen J. T., Cutter G. A., Daniels C., Dehairs F., Deng F., Dieu H. T., Duggan B., Dulaquais G., Dumousseaud C., EchevoyenSanz Y., Edwards R. L., Ellwood M., Fahrbach E., Fitzsimmons J. N., Flegal A. R., Fleisher M. Q., van de Flierdt T., Frank M., Friedrich J., Fripiat F., Fröllje H., Galer S. J. G., Gamo T., Ganeshram R. S., GarciaOrellana J., GarciaSolsona E., GaultRingold M., George E., Gerringa L. J. A., Gilbert M., Godoy J. M., Goldstein S. L., Gonzalez S. R., Grissom K., Hammerschmidt C., Hartman A., Hassler C. S., Hathorne E. C., Hatta M., Hawco N., Hayes C. T., Heimbürger L.E., Helgoe J., Heller M., Henderson G. M., Henderson P. B., van Heuven S., Ho P., Horner T. J., Hsieh Y.T., Huang K.F., Humphreys M. P., Isshiki K., Jacquot J. E., Janssen D. J., Jenkins W. J., John S., Jones E. M., Jones J. L., Kadko D. C., Kayser R., Kenna T. C., Khondoker R., Kim T., Kipp L., Klar J. K., Klunder M., Kretschmer S., Kumamoto Y., Laan P., Labatut M., Lacan F., Lam P. J., Lambelet M., Lamborg C. H., Le Moigne F. A. C., Le Roy E., Lechtenfeld O. J., Lee J.M., Lherminier P., Little S., LópezLora M., Lü Y., Masqué P., Mawji E., McClain C. R., Measures C., Mehic S., Barraqueta J.L. M., van der Merwe P., Middag R., Mieruch S., Milne A., Minami T., Moffett J. W., Moncoiffe G., Moore W. S., Morris P. J., Morton P. L., Nakaguchi Y., Nakayama N., Niedermiller J., Nishioka J., Nishiuchi A., Noble A., Obata H., Ober S., Ohnemus D. C., van Ooijen J., OSullivan J., Owens S., Pahnke K., Paul M., Pavia F., Pena L. D., Peters B., Planchon F., Planquette H., Pradoux C., Puigcorbe V., Quay P., Queroue F., Radic A., Rauschenberg S., Rehkämper M., Rember R., Remenyi T., Resing J. A., Rickli J., Rigaud S., Rijkenberg M. J. A., Rintoul S., Robinson L. F., Roca-Martí M., Rodellas V., Roeske T., Rolison J. M., Rosenberg M., Roshan S., van der Loeff M. M. R., Ryabenko E., Saito M. A., Salt L. A., Sanial V., Sarthou G., Schallenberg C., Schauer U., Scher H., Schlosser C., Schnetger B., Scott P., Sedwick P. N., Semiletov I., Shelley R., Sherrell R. M., Shiller A. M., Sigman D. M., Singh S. K., Slagter H. A., Slater E., Smethie W. M., Snaith H., Sohrin Y., Sohst B., Sonke J. E., Speich S., Steinfeldt R., Stewart G., Stichel T., Stirling C. H., Stutsman J., Swarr G. J., Swift J. H., Thomas A., Thorne K., Till C. P., Till R., Townsend A. T., Townsend E., Tuerena R., Twining B. S., Vance D., Velazquez S., Venchiarutti C., VillaAlfageme M., Vivancos S. M., Voelker A. H. L., Wake B., Warner M. J., Watson R., van Weerlee E., Weigand M. A., Weinstein Y., Weiss D., Wisotzki A., Woodward E. M. S., Wu J., Wu Y., Wuttig K., Wyatt N., Xiang Y., Xie R. C., Xue Z., Yoshikawa H., Zhang J., Zhang P., Zhao Y., Zheng L., Zheng X.Y., Zieringer M., Zimmer L. A., Ziveri P., Zunino P. & Zurbrick C. (2018). The GEOTRACES Intermediate Data Product 2017. *Chemical Geology*, 493, 210–223. <https://doi.org/10.1016/j.chemgeo.2018.05.040>

Schmitz. (1987). Barium, equatorial high productivity, and the northward wandering of the Indian continent. *Paleoceanography*, 2(1), 63–77. <https://doi.org/10.1029/PA002i001p00063>

Schroeder, J. O., Murray, R. W., Leinen, M., Pflaum, R. C., & Janecek, T. R. (1997). Barium in equatorial Pacific carbonate sediment: Terrigenous, oxide, and biogenic associations. *Paleoceanography*, 12(1), 125–146. <https://doi.org/10.1029/96PA02736>.

Serno, S., Winckler, G., Anderson, R. F., Hayes, C. T., Ren, H., Gersonde, R., & Haug, G. H. (2014). Using the natural spatial pattern of marine productivity in the Subarctic North Pacific to evaluate paleoproductivity proxies. *Paleoceanography*, 29(5), 438-453. <https://doi.org/10.1002/2013PA002594>

- Sherwen, T., Chance, R. J., Tinel, L., Ellis, D., Evans, M. J., & Carpenter, L. J. (2019). A machine-learning-based global sea-surface iodide distribution. *Earth System Science Data*, 11(3), 1239–1262. <https://doi.org/10.5194/essd-11-1239-2019>
- Sinclair, D. J., & McCulloch, M. T. (2004). Corals record low mobile barium concentrations in the Burdekin River during the 1974 flood: Evidence for limited Ba supply to rivers? *Palaeogeography, Palaeoclimatology, Palaeoecology*, 214(1), 155–174. <https://doi.org/10.1016/j.palaeo.2004.07.028>
- Singh, S. P., Singh, S. K., & Bhushan, R. (2013). Internal cycling of dissolved barium in water column of the Bay of Bengal. *Marine Chemistry*, 154, 12–23. <https://doi.org/10.1016/j.marchem.2013.04.013>
- [Singh, A. K., Marcantonio, F., & Lyle, M. \(2020\). An assessment of xsBa flux as a paleoproductivity indicator and its water-depth dependence in the easternmost equatorial Pacific Ocean. *Paleoceanography and Paleoclimatology*, 35\(12\), e2020PA003945.](#)
- Stewart, J. A., Li, T., Spooner, P. T., Burke, A., Chen, T., Roberts, J., Rae, J. W. B., Peck, V., Kender, S., Liu, Q., & Robinson, L. F. (2021). Productivity and Dissolved Oxygen Controls on the Southern Ocean Deep-Sea Benthos During the Antarctic Cold Reversal. *Paleoceanography and Paleoclimatology*, 36(10), e2021PA004288. <https://doi.org/10.1029/2021PA004288> <https://doi.org/10.1029/2021PA004288>
- Stroobants, N., Dehairs, F., Goeyens, L., Vanderheijden, N., & Van Grieken, R. (1991). Barite formation in the Southern Ocean water column. *Marine Chemistry*, 35(1), 411–421. [https://doi.org/10.1016/S0304-4203\(09\)90033-0](https://doi.org/10.1016/S0304-4203(09)90033-0)
- Talley, L. D. (1991). An Okhotsk Sea water anomaly: implications for ventilation in the North Pacific. *Deep Sea Research Part A. Oceanographic Research Papers*, 38, S171-S190. [https://doi.org/10.1016/S0198-0149\(12\)80009-4](https://doi.org/10.1016/S0198-0149(12)80009-4)
- [Talley, L. D. \(2008\). Freshwater transport estimates and the global overturning circulation: Shallow, deep and throughflow components. *Progress in Oceanography*, 78\(4\), 257-303. <https://doi.org/10.1016/j.pocean.2008.05.001>](#)
- [Talley, L. D., Pickard, G. L., & Emery, W. J. \(Eds.\). \(2011\). *Descriptive physical oceanography: An introduction* \(6th ed\). Academic Press.](#)
- Waldeck, A. R., Hemingway, J. D., Yao, W., Paytan, A., & Johnston, D. T. (2022). The triple oxygen isotope composition of marine sulfate and 130 million years of microbial control. *Proceedings of the National Academy of Sciences*, 119(31), e2202018119. <https://doi.org/10.1073/pnas.2202018119>
- Whitmore, L. M., Shiller, A. M., Horner, T. J., Xiang, Y., Auro, M. E., Bauch, D., Dehairs, F., Lam, P. J., Li, J., Maldonado, M. T., Mears, C., Newton, R., Pasqualini, A., Planquette, H., Rember, R., & Thomas, H. (2022). Strong Margin Influence on the Arctic Ocean Barium Cycle Revealed by Pan-Arctic Synthesis. *Journal of Geophysical Research: Oceans*, 127(4), e2021JC017417. <https://doi.org/10.1029/2021JC017417> <https://doi.org/10.1029/2021JC017417>

Wyatt, N. J., Milne, A., Woodward, E. M. S., Rees, A. P., Browning, T. J., Bouman, H. A., Worsfold, P. J., & Lohan, M. C. (2014). Biogeochemical cycling of dissolved zinc along the GEOTRACES South Atlantic transect GA10 at 40 S. *Global Biogeochemical Cycles*, 28(1), 44-56. <https://doi.org/10.1002/2013GB004637>

Zhang, Z., Yu, Y., Hathorne, E. C., Vieira, L. H., Grasse, P., Siebert, C., Rahlf, P., & Frank, M. (2023). Decoupling of Barium and Silicon at the Congo River-dominated Southeast Atlantic Margin: Insights from Combined Barium and Silicon Isotopes. *Global Biogeochemical Cycles*, e2022GB007610. <https://doi.org/10.1029/2022GB007610>

Zweng, M.M, J.R. Reagan, D. Seidov, T.P. Boyer, R.A. Locarnini, H.E. Garcia, A.V. Mishonov, O.K. Baranova, K.W. Weathers, C.R. Paver, and I.V. Smolyar (2018). World Ocean Atlas 2018, Volume 2: Salinity. A. Mishonov, Technical Editor, NOAA Atlas NESDIS 82, 50pp. <http://www.nodc.noaa.gov/OC5/indprod.html>